Published for SISSA by Springer

Received: July 8, 2022
Revised: November 25, 2022
Accepted: November 28, 2022
Published: December 29, 2022

Top-philic dark matter in a hybrid KSVZ axion framework

Anupam Ghosh,[a,b] **Partha Konar**[a] **and Rishav Roshan**[c]

[a] *Theoretical Physics Division, Physical Research Laboratory, Shree Pannalal Patel Marg, Ahmedabad 380009, Gujarat, India*
[b] *Discipline of Physics, Indian Institute of Technology, Palaj, Gandhinagar 382424, Gujarat, India*
[c] *Department of Physics, Kyungpook National University, Daegu, 41566, Korea*

E-mail: anupam@prl.res.in, konar@prl.res.in, rishav.roshan@gmail.com

Abstract: We explore a two-component dark matter scenario in an extended Kim-Shifman-Vainshtein-Zakharov (KSVZ) axion framework. This hybrid setup incorporates an extra $SU(2)_L$ complex singlet scalar whose lightest component plays the role of one of the dark matter, while the QCD axion of the KSVZ model acts as a second dark matter candidate. In this work, we focus on accentuating the role of vector-like quark that naturally emerges in the KSVZ extension on the dark matter and collider phenomenology. Here, we demonstrate that the presence of this colored particle can significantly affect the allowed dark matter parameter space of the scalar dark matter by opening up additional co-annihilation as well as the direct detection channels. Moreover, the interaction between the color particle with the top quark and scalar dark matter provides a unique topology to generate a boosted-top pair with considerable missing transverse momentum at the LHC. Using jet substructure variables and multivariate analysis, here we show that one can already exclude a vast region of parameter space with 139 fb^{-1} integrated luminosity at 14 TeV LHC.

Keywords: Dark Matter at Colliders, Jets and Jet Substructure

ArXiv ePrint: 2207.00487

https://doi.org/10.1007/JHEP12(2022)167

JHEP12(2022)167

Contents

JHEP12(2022)167

1 Introduction

The Standard Model (SM) of fundamental particles is one of the outstanding achievements of modern-day physics, which has been experimentally verified at many frontiers. Ever since the discovery of the Higgs boson [1, 2], the last missing piece of SM, the particle physics community is eagerly scrutinizing collider data to witness if nature can offer a glimmer of hope in the ongoing hunt for new physics. Physics beyond the SM (BSM) is envisaged as inevitable since SM still fails to account for various issues to give us a fully coherent description of nature. Some of the principal concerns are related to the Strong CP problem [3, 4], the existence of the dark matter (DM) [5, 6] in the Universe, non-zero but minuscule neutrino masses [7–9], matter-antimatter asymmetry of the Universe [10, 11] etc. The incapability of the SM in explaining these issues motivates us to look at possible extensions accommodating these aspects.

Different celestial observational evidence [5, 6] at diverse length scales suggests the existence of a non-baryonic, non-luminous, gravitationally interacting form of matter in the Universe, which is popularly known as the *dark matter*. Precision measurement of anisotropies in cosmic microwave background radiation (CMBR) in Wilkinson Microwave Anisotropy Probe (WMAP) [12] and PLANCK [13] played a crucial role in providing us with a valuable estimate of the present abundance of DM relic density. Despite these shreds of evidence in different formats, the particle nature of the DM is still obscured from us. Different

DM paradigms exist in the literature attempting to explain the DM's particle nature. Some of the most popular ones are weakly interacting massive particles (WIMP) [14–21], feebly interacting massive particle (FIMP) [22–29], asymmetric dark matter models [30, 31], models with axion or axion-like particle (ALP) DM [32–35] etc. Although these models can explain the DM relic density of the Universe, their parameter spaces are restricted from different experimental searches. For instance, WIMP dark matter is severely constrained from null detection of the DM in the collider searches [36, 37] as well as the direct [38–41] and indirect [42–44] search experiments.

Interestingly such a null outcome in experimental searches can instead be an indication of a much richer dark sector, and the dark sector can possibly be composed of more than one component of DM. In recent times, there have been several proposals for a multicomponent dark matter [45–58] where the dark sector is made up of different DM components. For example, one can think of a scenario with WIMP-WIMP [45–49] dark matter candidates, WIMP-FIMP [50–52] dark matter candidates, FIMP-FIMP [53, 54] dark matter candidates, WIMP-axion [55, 56] dark matter candidates, etc. In the present work, we aim to explore one such scenario where the dark sector constitutes a WIMP-type dark matter, and the QCD axion plays the role of a second dark matter.

The minimal extension of the SM that can accommodate a WIMP dark matter is its extension by a scalar singlet field with a Higgs portal interaction [59–61]. Here, the DM is assumed to have an odd charge under a discrete unbroken Z_2 symmetry that guarantees its stability. This particular DM scenario is in tension with direct search experiments. The recent direct detection data from the XENON1T experiment [41] has nearly ruled out the DM with mass below 1 TeV [46, 48, 62] apart from the near Higgs resonance region. Reviving this sub-TeV parameter space of the scalar singlet DM could be an exciting undertaking since it can open the possibility of its testing at different frontiers like direct, indirect, and collider searches. One possible way to revive this sub-TeV parameter space is to embed this scalar DM in a two-component framework [46, 48]. With various extensions of two-component DM with a scalar singlet already in place, an interesting exercise could explore the insertion of a scalar singlet in a QCD axion DM framework, as it can enlarge the scalar singlet DM parameter space and can also provide rich collider phenomenology.

Extension of the SM with a global Peccei-Quinn (PQ) symmetry [3, 4] provides solutions for two of the critical issues discussed above in one go, i.e., the *Strong CP problem* and the existence of *dark matter*. This global symmetry is expected to be broken at a scale much larger than the Electroweak (EW) scale. The breaking of $\mathrm{U}(1)_{\mathrm{PQ}}$ predicts a pseudo-Goldstone particle, popularly known as the *QCD axion*, that is not absolutely stable but can have a lifetime much greater than the age of the Universe [32–35] to play the role of DM. There are primarily three different QCD axion models that can simultaneously explain the presence of the DM in the Universe and solve the Strong CP problem. The (i) Peccei-Quinn-Weinberg-Wilczek (PQWW) [3, 63, 64] model introduces an additional singlet scalar that also obtains a non-zero vacuum expectation value (vev) at the time of EW phase transition. This setup is already ruled out from the experiments. The (ii) Kim-Shifman-Vainshtein-Zakharov (KSVZ) [65, 66] model introduces an extra colored particle together with a complex scalar that breaks the PQ symmetry. Anomaly-free

JHEP12(2022)167

condition is ensured by the introduction of vector-like quarks (VLQ). Finally, the (iii) Dine-Fischler-Srednicki-Zhitnitsky (DFSZ) [67, 68] model incorporates an additional Higgs field apart from the PQ breaking scalar. It is also interesting to point out that the breaking of PQ symmetry in these models also leaves a remnant Z_2 symmetry that remains intact. If such a setup is extended with an extra particle that also carries a non-trivial Z_2, then this unbroken symmetry can naturally ensure its stability. This motivates us to study two-component DM scenarios in these models.

In the present work, we aim to explore a hybrid KSVZ scenario, where an extra complex scalar singlet extends the particle spectrum of the KSVZ setup in addition to the usual complex scalar that breaks the PQ symmetry. As mentioned above, the breaking of $\mathrm{U}(1)_{\mathrm{PQ}}$ symmetry in the KSVZ construction leaves remnant Z_2 symmetry which remains unbroken throughout, and the VLQ present in the setup carries an odd charge under it. If the model is extended by a complex scalar that also holds a non-trivial charge under the same Z_2, the lightest component of the scalar can play the role of the second dark matter, making the dark sector two-component.

Note that our setup is similar to the one considered in [55, 56] but with some crucial differences. For example, the present framework considers an up-type VLQ rather than a down-type VLQ, and it opens up a non-trivial possibility in collider analysis. Current construction also aims to explore the possibility of DM effective annihilations (including the DM co-annihilation with the vector-like quark as well as the annihilation of the vector-like quark to the SM particles) to the SM particles in obtaining the correct relic density of the scalar (WIMP) DM. Next, both [55, 56] did not consider the VLQ's contribution to the DM-nucleon spin-independent scattering, which can play a crucial role in the DM phenomenology of WIMP dark matter. This feature of DM effective annihilation to the SM particles, as well as the role of the VLQ in the tree level spin-independent DM-nucleon scattering, was also discussed in [62]. Ref. [62] featured a VLQ doublet and VLQ singlet fermions, unlike ours with a singlet VLQ which naturally occurs in a KSVZ scenario. We also want to emphasize that, although [55, 56, 62] featured some discussions on the collider aspect of this kind of setup, none of them explored it in detail. In the present work, we also perform an exhaustive colliders analysis and aim to find out the relevant parameter space, which would not only validate the dark matter phenomenology but also be consistent with the collider searches.

The paper is organized as follows. We introduce our model in section 2 where the particle spectrum together with their charges under different symmetry groups have been discussed. Various theoretical and experimental constraints in our model are presented in section 3. In section 4 we discuss the dark matter phenomenology of the model. The collider analysis and the result based on multivariate analysis are presented in section 5. Finally, we summarize our findings in section 6.

2 The model

As stated in the introduction, the present work aims to study dark matter and collider phenomenology in a hybrid KSVZ framework of QCD axion. As is well known, the vanilla

JHEP12(2022)167

	η	S	Ψ
$\mathrm{SU}(3)_C$	1	1	3
$\mathrm{SU}(2)_L$	1	1	1
$\mathrm{U}(1)_Y$	0	0	2/3
$\mathrm{U}(1)_{\mathrm{PQ}}$	2	1	1

Table 1. Particle contents and their respective charge assignments under different symmetry groups.

KSVZ model requires a complex scalar singlet η that breaks a global symmetry, popularly known as $\mathrm{U}(1)_{\mathrm{PQ}}$. In addition, this model also demands a $\mathrm{SU}(2)_L$ singlet colored fermion Ψ with a $+1$ unit of $\mathrm{U}(1)_{\mathrm{PQ}}$ charge. This extra quark is vector-like and hence does not introduce any chiral anomaly. In addition, the hybrid KSVZ model also introduces an additional complex singlet scalar S charged under the $\mathrm{U}(1)_{\mathrm{PQ}}$. The BSM fermion and scalar content of the model and their respective charges are listed in table 1. The most general renormalizable and gauge-invariant Lagrangian for the present setup can be written as,

$$-\mathcal{L}^{\mathrm{VLQ}} = f_i S\overline{\Psi}_L u_{iR} + f_\Psi \eta \overline{\Psi}_L \Psi_R + h.c., \tag{2.1}$$

where, u_R represents right-handed up-type quarks in the SM with $i = u, c, t$. Here, L and R denote left- and right-handed projections. Note that the hypercharge of the newly introduced VLQ depends on its interaction with SM quarks. The relevance of introducing an up-type VLQ in this setup will be clear once we discuss the DM and collider phenomenologies in sections 4 and 5 respectively.

Moving on to the scalar part of the Lagrangian, the most general renormalizable scalar potential of our model, $V(H, \eta, S)$ can be written as,

$$\begin{aligned} V(H,\eta,S) = {} & \lambda_H(|H|^2 - v_H^2/2)^2 + \lambda_\eta(|\eta|^2 - F_a^2/2)^2 + \lambda_{\eta H}(|H|^2 - v_H^2/2)(|\eta|^2 - F_a^2/2) \\ & + \mu_S^2|S|^2 + \lambda_S|S|^4 + \lambda_{SH}|H|^2|S|^2 + \lambda_{S\eta}|\eta|^2|S|^2 + [\epsilon_S \eta^* S^2 + h.c]. \end{aligned} \tag{2.2}$$

After the breaking of both $\mathrm{U}(1)_{\mathrm{PQ}}$ and the SM gauge symmetry, the different scalars involved in the present setup take the following form,

$$H = \begin{pmatrix} 0 \\ \frac{1}{\sqrt{2}}(v_H + h_0) \end{pmatrix}, \quad \eta = e^{\frac{ia}{F_a}} \frac{(F_a + \sigma_0)}{\sqrt{2}}, \quad S = \frac{S_1 + iS_2}{\sqrt{2}}, \tag{2.3}$$

where v_H denotes the vacuum expectation value (vev) of H obtained after the electroweak symmetry breaking (EWSB) and F_a represents the $\mathrm{U}(1)_{\mathrm{PQ}}$ breaking scale. It is to be noted that, after the breaking of both symmetries, a non-zero $h_0 - \sigma_0$ mixing leads to the following mass terms:

$$M^2 \equiv \begin{pmatrix} 2v_H^2\lambda_H & F_a v_H \lambda_{\eta H} \\ F_a v_H \lambda_{\eta H} & 2F_a^2 \lambda_\eta \end{pmatrix}. \tag{2.4}$$

The mass matrix can be diagonalised using

$$\begin{pmatrix} h_0 \\ \sigma_0 \end{pmatrix} = \begin{pmatrix} \cos\theta_m & \sin\theta_m \\ -\sin\theta_m & \cos\theta_m \end{pmatrix} \begin{pmatrix} h \\ \sigma \end{pmatrix} \tag{2.5}$$

JHEP12(2022)167

where the mixing angle is given by,

$$\tan(2\theta_m) = \frac{F_a v \lambda_{\eta H}}{F_a^2 \lambda_\eta - v^2 \lambda_H}\,. \tag{2.6}$$

Finally, after diagonalization, the physical masses of the h and σ are given as,

$$M^2_{h,\sigma} = (\lambda_H v^2 + \lambda_\eta F_a^2) \pm \sqrt{(\lambda_H v^2 - \lambda_\eta F_a^2)^2 + F_a^2 v^2 \lambda^2_{\eta H}}\,. \tag{2.7}$$

Next, as an artifact of two different symmetry breakings, the masses of the different components of the S can be expressed as,

$$M^2_{S_{1,2}} = \frac{1}{2}\left(2\mu_S^2 + v_H^2 \lambda_{SH} + F_a^2 \lambda_{S\eta} \mp 2\sqrt{2}\epsilon_s F_a\right). \tag{2.8}$$

Notice that the presence of the term proportional to ϵ_S in eq. (2.2) plays a crucial role in generating the mass splitting among the components of S. Subsequently, the mass of the VLQ is given as,

$$M_\Psi = f_\Psi \frac{F_a}{\sqrt{2}}. \tag{2.9}$$

At this stage, it is interesting to point out that, even after the breaking of both the symmetries, there still exists a remnant Z_2 symmetry under which both the Lagrangian as well as the scalar potential remains invariant. This remnant Z_2 can remain intact if S does not acquire a non-zero vev. Under such a scenario, the lightest neutral component of S can provide a vital DM candidate.

Finally, the setup also contains a pseudo-Nambu Goldstone boson a, associated with scalar η, popularly known as *axion*. The axion obtains a mass as a result of non-perturbative QCD effects given as [32, 34],

$$m_a \simeq 0.6 \text{ meV} \times \left(\frac{10^{10} \text{ GeV}}{F_a}\right). \tag{2.10}$$

Note that a suitable choice of decay constant F_a can adjust the fraction of which QCD axion can contribute toward the relic density of the dark matter. That makes the preset setup a tunable two-component dark matter scenario. The role of QCD axion as a DM candidate and its constraints are elaborated in section 4. Now with the knowledge of all the particles and their interactions in this hybrid KSVZ setup, we are in a position to list the set of independent parameters important for the dark matter and collider phenomenology:

$$\{M_\Psi, M_{S_1}, M_{S_2}, M_\sigma, F_a, \lambda_{SH}, \lambda_{S\eta}, f_i\}.$$

JHEP12(2022)167

3 Experimental and theoretical constraints

The extended KSVZ model under consideration is subjected to various theoretical as well as experimental constraints. In this section, we summarize all the relevant ones.

- **Stability and perturbativity.** The scalar sector is extended over the vanilla model. Hence, different scalars in the present setup can help stabilize the electroweak vacuum. The stability of the electroweak vacuum also demands that the scalar potential should be bounded from below in all the field directions of the field space. On the other hand, a perturbative theory demands that the model parameters should obey:

$$|\lambda_i| < 4\pi \text{ and } |g_i|, |y|, |f_i| < \sqrt{4\pi}, \tag{3.1}$$

  where g_i and y are the SM gauge and Yukawa couplings, whereas f_i are Yukawa couplings involving different BSM fields, respectively.

- **Relic density, direct and indirect detection of DM.** For any dark matter model, it is essential to satisfy the observed abundance of DM relics from the precision measurement in the Planck experiment [69],

$$\Omega_{\rm DM}h^2 = 0.120 \pm 0.001. \tag{3.2}$$

  Apart from DM relic density, the DM-nucleon scattering cross-section is also constrained by various direct search experiments like LUX [38], PandaX-II [39, 40], and XEXON1T [41]. Finally, the DM annihilation to the SM particles are also subjected to the constraints coming from the indirect search experiments like PAMELA [42], Fermi-LAT [44], MAGIC [43] etc. Nonetheless, in all these cases, one also needs to take care of the multi-component nature of DM in our extended scenario, which is further discussed in section 4.

- **Flavor constraints.** The Yukawa interactions of the complex singlet scalar S with VLQ and the SM right-handed quarks like u and c in the present setup can contribute towards the $D^0 - \bar{D}^0$ mixing [70]. The measured value of the D-meson mass splitting significantly constrained this mixing. The Feynmann diagrams that contribute to this mixing are shown in figure 15; each diagram has four possible configurations with a total of sixteen diagrams. Effective operator contributing to this mixing in the present setup can be expressed as

$$\mathcal{L}_{\rm eff} = \frac{\tilde{z}}{M_\Psi^2}\bar{u}_R^\alpha \gamma^\mu c_R^\alpha \bar{u}_R^\beta \gamma_\mu c_R^\beta, \tag{3.3}$$

  where

$$\tilde{z} = -\frac{f_u^2 f_c^2}{96\pi^2}[g_\psi(M_{S_1}^2/M_\Psi^2) + g_\psi(M_{S_2}^2/M_\Psi^2) - 2g_\psi(M_{S_1}M_{S_2}/M_\Psi^2)]. \tag{3.4}$$

  Here $g_\Psi(x) = 24x f_6(x) + 12\tilde{f}_6(x)$ where the expressions of f_6 and $\tilde{f}_6$ can be found in [71]. The measurement of the D-meson mass splitting demands $|\tilde{z}| \lesssim 5.7 \times 10^{-7}(M_\Psi/\text{TeV})^2$ [70, 71]

JHEP12(2022)167

- **LHC diphoton searches.** As a result of mixing between h and σ, all the tree level interactions with the SM Higgs get modified. In such a case, the signal strength in the di-photon channel takes a form:

$$\mu_{\gamma\gamma} = c_\theta^2 \frac{BR_{h\to\gamma\gamma}}{BR^{\rm SM}_{h\to\gamma\gamma}} \simeq c_\theta^2 \frac{\Gamma_{h\to\gamma\gamma}}{\Gamma^{\rm SM}_{h\to\gamma\gamma}}. \tag{3.5}$$

  LHC sets a limit on this new mixing angle as $|\sin\theta| \leq 0.36$ [72].

- **Invisible Higgs decay.** Involvement of the new interactions of SM Higgs with various BSM particles in the present setup can lead to its new decay modes if kinematically allowed. These extra decays of Higgs can contribute toward invisible Higgs decay. In such a situation, we need to employ the bound on the invisible Higgs decay width as [73]:

$$Br(h \to \text{Invisible}) \equiv \frac{\Gamma(\text{h} \to \text{Invisible})}{\Gamma(\text{h} \to \text{SM}) + \Gamma(\text{h} \to \text{Invisible})} < 0.11. \tag{3.6a}$$

  In the case of light DM, the Higgs can decay to a pair of it when kinematically allowed. However, in our present analysis, we primarily focus on the parameter space where $m_i > \frac{m_h}{2}$ so the above constraint is not applicable.

- **Direct collider constraints.** Due to the presence of colored vector-like quarks, the present model is subjected to various collider constraints. Being non-trivially charged under the $\text{U}(1)_{\text{PQ}}$ allows the VLQ to couple with the complex scalar and the SM up type quarks. If kinematically allowed, the heavier states can always decay into the DM and an SM quark. Therefore a generic collider signature of this model contains a considerable amount of missing (transverse) energy from the escape of final DM particles from detection at the detector.

  Vector-like fermion can be pair produced through electroweak interaction performed at CERN's Large Electron Positron Collider (LEP):

$$e^+e^- \to \gamma^*, Z \to \Psi\bar{\Psi} \tag{3.7}$$

  The interaction between vector-like fermion, light SM quarks, and the DM can lead to the decay of Ψ to a light quark associated with DM at LEP if kinematically allowed. The reinterpreted LEPII results of squark search [74, 75] exclude the mass of Ψ up to 100 GeV. Such constraint is incorporated in our final exclusion plots. Please follow the brown region in figure 10. Similar searches were also carried out at the LHC. In a recent ATLAS search, the vector-like mediator is searched while it decays into an invisible particle and light quark up (charm) when the mass difference between the mediator and DM is less than the top quark mass. The green region in figure 10 is excluded from the reinterpreted result [74] of the ATLAS search [76] for multijet (2–6 jets) plus missing transverse momentum at center-of-mass (CM) energy $\sqrt{s} = 8$ TeV with an integrated luminosity of 20.3 fb^{-1}. Exploring a larger mass difference between the mediator and DM candidate, top-antitop plus missing transverse momentum signal

JHEP12(2022)167

has been extensively studied by both CMS and ATLAS collaborations, particularly superpartners searches of the top quark [77–85] and some dedicated dark matter searches [37]. The vector-like mediator can be pair produced at the LHC mainly through strong interaction and then decay into an up-type quark and invisible particle. So, the search for a top pair along with the missing transverse momentum signature by ATLAS and CMS can be reinterpreted to exclude some of the parameter spaces of this model. The CMS analysis [85] is reinterpreted in ref. [86] at 13 TeV LHC for an integrated luminosity of 35.9 fb^{-1}, assuming vector-like mediator decay with 100% branching fraction into the top and invisible particle. In their analysis, the signal consists of two oppositely charged isolated leptons from leptonic decays of both top and anti-top. The signal also consists of at least two hard jets; one of them is b-tagged and a large missing transverse momentum. The olive region in figure 10 is the exclusion region (2σ) obtained from this analysis.

The existing LHC search relies on finding the top pair based on two hard leptons and a b-tagged jet. It is evident that the sensitivity of such detection deteriorates when these tops are boosted, especially while decaying from a heavy mother particle. We propose an alternative search strategy in this work by recognizing these boosted double top jets with a large missing transverse energy signature using jet substructure variables and multivariate analysis. We are examining the spectrum where the mass difference between vector-like mediator and DM is larger than the mass of the top quark such that on-shell decay into the top is possible. Our search strategy helps to explore the significant parameter space of this model that gives observed relic density of DM and also allowed from the direct-detection experiment with the current luminosity of the LHC.

4 Dark matter phenomenology

In this section, we aim to elaborate on the DM phenomenology of the model under consideration. As discussed earlier, the setup is a hybrid of the KSVZ model that includes an extra complex scalar (S) whose lightest component (S_1) plays the role of one of the DM while the part of the second DM is played by the QCD axion of the KSVZ setup. The involvement of the two DMs in this extended KSVZ scenario makes the layout a two-component DM system. Besides the QCD axion, the KSVZ setup naturally demands a presence of an extra colored fermionic $\text{SU}(2)_L$ singlet. This fermion plays a non-trivial role in the DM phenomenology and the collider searches of the DM as it talks directly to it through the Yukawa interaction given in eq. (2.1). Next, we discuss the DM phenomenology of both the DM candidates of the present model.

4.1 Relic density and DM detection

Apart from providing a solution to the *strong CP problem*, another interesting consequence of introducing a PQ symmetry is the emergence of the Nambu Goldstone boson, popularly known as *axion*. If the breaking scale (F_a) of the PQ symmetry is chosen appropriately, the resulting axion can be light as well as stable. This QCD axion can be an excellent DM

JHEP12(2022)167

candidate in such a scenario. Axions can be produced non-thermally as a result of the misalignment mechanism. Here, the axion field begins to coherently oscillate around the minimum of the PQ vacuum when its mass becomes comparable to the Hubble parameter. This coherent oscillation of the axion field behaves like a cold matter in the Universe. The relic density of the axion in such a case is approximately given by [55, 56, 87],

$$\Omega_a h^2 \simeq 0.18\, \theta_a^2 \left(\frac{F_a}{10^{12}\text{GeV}}\right)^{1.19}. \tag{4.1}$$

Here, θ_a represents the initial misalignment angle of the axion.

For the case of the scalar DM, we consider the mass hierarchy $M_{S_2} > M_{S_1}$ such that the lightest scalar component represents the second DM candidate. Its interactions with the SM Higgs and the VLQ keep it in equilibrium with the thermal bath in the early Universe. As the temperature of the Universe drops below the DM mass, its production from the thermal bath stops while its annihilation of the SM particle continues. Once the Universe's expansion rate becomes larger than the interaction rate of the DM, its annihilation to the SM bath also stops, and its abundance freezes out. DM can annihilate to the SM particles through: (a) its contact interactions, (b) Higgs-mediated channels[1] and (c) VLQ mediated channels (as a result of Yukawa interaction given in eq. (2.1)). The presence of the Yukawa interaction also allows the DM to co-annihilate if the mass-splitting between the DM and newly introduced quark is sufficiently small. Note that as the VLQ and S_2 share the same Z_2 charge similar to the DM, their annihilations would also be important for evaluating the effective annihilation cross-section. In appendix A, we present all the important annihilation and co-annihilation channels of the DM that are crucial in determining its final relic abundance.[2] Once all the important annihilation and co-annihilation channels are identified, one can use them to determine the final relic density of the DM, which can be expressed as [60],

$$\Omega_{S_1} h^2 = \frac{1.09 \times 10^9\ \text{GeV}^{-1}}{g_*^{1/2}\ M_{Pl}} \frac{1}{J(x_f)}, \tag{4.2}$$

where $J(x_f)$ is given by,

$$J(x_f) = \int_{x_f}^{\infty} \frac{\langle\sigma|v|\rangle_{\text{eff}}}{x^2}\ \text{dx}. \tag{4.3}$$

$\langle\sigma|v|\rangle_{\text{eff}}$ in eq. (4.3) is the effective thermal average DM annihilation cross-sections including contributions from the co-annihilations and is given by,

$$\begin{aligned}\langle\sigma|v|\rangle_{\text{eff}} = {} & \frac{g_{s_1}^2}{g_{\text{eff}}^2}\sigma(\overline{S_1}S_1) + 2\frac{g_{s_1}g_{s_2}}{g_{\text{eff}}^2}\sigma(\overline{S_1}S_2)(1+\Delta_{12})^{3/2}\ \exp[-x\Delta_{12}] + 2\frac{g_{s_1}g_{\Psi}}{g_{\text{eff}}^2}\sigma(\overline{S_1}\Psi)(1+\Delta_{\Psi})^{3/2} \\ & \exp[-x\Delta_{\Psi}] + \frac{g_{S_2}^2}{g_{\text{eff}}^2}\sigma(\overline{S_2}S_2)(1+\Delta_{12})^3\ \exp[-2x\Delta_{12}] + \frac{g_{\Psi}^2}{g_{\text{eff}}^2}\sigma(\overline{\Psi}\Psi)(1+\Delta_{\Psi})^3 \\ & \exp[-2x\Delta_{\Psi}].\end{aligned} \tag{4.4}$$

[1] From eq. (2.7), it is evident that until and unless λ_η is very small, M_σ will remain much heavier than M_h and hence the σ mediated annihilation channels be very much suppressed.

[2] Just for completeness we have also shown the DM annihilation to the axion final states. These annihilations are highly suppressed and do not contribute towards the relic density of scalar dark matter. This is because most of the vertices involved in these annihilation cross-sections are either proportional to $1/F_a$ or $\frac{\sin\theta}{F_a}$ or $\frac{\epsilon_S}{F_a}$ or ϵ_S.

JHEP12(2022)167

In the equation above, g_{s_1}, g_{s_2} and g_Ψ are the spin degrees of freedom for S_1, S_2 and Ψ. Here, $x = \frac{M_{S_1}}{T}$ representing dimensionless parameter with inverse of temperature, while Δ_Ψ and Δ_{12} are two dimensionless parameters qualifying mass splittings from dark scalar candidate:

$$\Delta_\Psi = \frac{M_\Psi - M_{S_1}}{M_{S_1}};\ \Delta_{12} = \frac{M_{S_2} - M_{S_1}}{M_{S_1}}. \tag{4.5}$$

The effective degrees of freedom in eq. (4.4) is given by,

$$g_{\text{eff}} = g_{s_1} + g_{s_2}(1+\Delta_{12})^{3/2}\ \exp[-x\Delta_{12}] + g_\Psi(1+\Delta_\Psi)^{3/2}\ \exp[-x\Delta_\Psi]. \tag{4.6}$$

In the following analysis, we first generate the model using FeynRules [88] and then implement it in `micrOMEGAs` -v5 [89] to find the region of parameter space that corresponds to correct relic abundance for our scalar DM candidate in accordance with the relation,

$$\Omega_{\text{T}}h^2 = \Omega_a h^2 + \Omega_{S_1}h^2, \tag{4.7}$$

where $\Omega_{\text{T}}h^2$ corresponds to the total relic density of the DM satisfying PLANCK constraints [69].

Next, the present model is subjected to the constraints coming from the direct search experiments for the dark matter. Experiments like LUX [38], PandaX-II [39, 40] looks for the DM recoil in the DM-nucleon scattering and subsequently provides a bound on the DM-nucleon scattering cross-section. Being a two-component DM system, the direct detection cross-section of the scalar DM should be rescaled as,

$$\sigma^{\text{SI}}_{S_{1,\text{eff}}} = \frac{\Omega_{S_1}}{\Omega_{\text{T}}}\sigma^{\text{SI}}_{S_1} \tag{4.8}$$

As mentioned earlier, due to the direct Yukawa interaction of the scalar DM with the up-quark, two other scattering processes contribute to the direct detection cross-section of the scalar apart from the usual SM Higgs-mediated scattering. In appendix A we listed all the scattering processes of the DM S_1 with the detector nucleon.

Finally, the model is also subjected to the constraints coming from the indirect search experiments. Indirect search experiments looking for an excess of gamma rays can help in probing the WIMP dark matter. DM particles can annihilate and produce SM particles, out of which photons (and also neutrinos), being electromagnetically neutral, have better chances of reaching the detector from the source without getting deflected. Experiments like PAMELA [42], Fermi-LAT [44], MAGIC [43] etc. look for such excess in order to confirm the particle nature of the DM. The present set up being a two-component DM scenario, the indirect detection cross-section of the scalar DM should be rescaled as well,

$$\sigma^{\text{ID}}_{S_{1,\text{eff}}} = \left(\frac{\Omega_{S_1}}{\Omega_{\text{T}}}\right)^2 \sigma^{\text{ID}}_{S_1}. \tag{4.9}$$

At this stage, it is worth commenting on some of the detection possibilities of the axion as a DM candidate. Several ongoing and proposed experiments rely on axion being a DM. All these experiments lean on different detection techniques. For example, ADMX [90]

JHEP12(2022)167

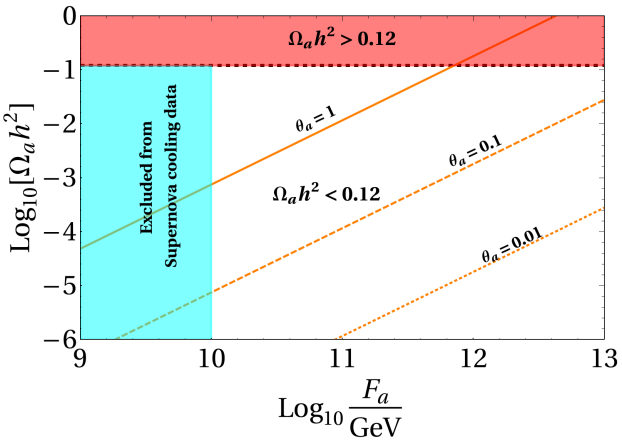

Figure 1. Variation of QCD axion relic density with the decay constant F_a for three different values of misalignment angles: $\theta_a = 1.0$ (solid), $\theta_a = 0.1$ (dashed), and $\theta_a = 0.01$ (dotted). Black thick dashed line corresponds to observed relic $\Omega_{\rm DM}h^2 = 0.12$. The cyan region is disallowed from the Supernova cooling data. The light pink region corresponds to the parameter space where the DM relic density remains overabundant.

searches for DM-photon conversion in the presence of the magnetic field. CASPEr [91] uses nuclear magnetic resonance to hunt for the axion DM; it is known that if the axion exists, it will modify Maxwell's equation. ABRACADABRA [92] utilizes this by using a toroidal magnet to source an effective electric current, and finally, MADMAX [93] is a proposed experiment that uses dielectrics haloscopes.

4.2 Parameter space of hybrid KSVZ axion framework

It is well known that the KSVZ model provides a DM in the form of QCD axion. For this axion to play the role of the DM or contributes sufficiently towards the relic density of the DM, the decay constant F_a should lie in the range,

$$10^{10}\ \text{GeV} \leq F_a \leq 10^{12}\ \text{GeV}. \tag{4.10}$$

The lower bound on F_a comes from the supernova cooling data [94] whereas the upper bound results from the overproduction of the axion or, in other words, the relic density of the axion become overabundant. To understand this, in figure 1 we study the variation of the axion relic density ($\Omega_a h^2$) with the decay constant for three different values of the misalignment angles i.e. $\theta_a = 1.0$ (solid), $\theta_a = 0.1$ (dashed), and $\theta_a = 0.01$ (dotted). The region in cyan is ruled out from the supernova cooling data, whereas the light pink region corresponds to the overproduced DM relic density. As can be seen from figure 1, for $\theta_a = 1.0$ and $F_a \simeq 10^{12}$ GeV, the axion alone can contribute 100% towards the relic density of the dark matter. Finally, the white region corresponds to the parameter space where QCD axion as a DM remains underabundant.

The present setup is an extended version of the KSVZ scenario, which contains an additional DM candidate as a singlet scalar. The presence of this extra DM here demands us to choose a parameter space for axion from figure 1 where the relic density of the axion

JHEP12(2022)167

remains underabundant so that the relic density of the axion together with the scalar can satisfy the Planck limit. For a demonstrative purpose, we fix $F_a = 10^{11}$ GeV and choose the misalignment angle as $\theta_a = 1$ for the rest of the analysis. This choice of F_a and θ_a corresponds to $\Omega_a h^2 = 0.012$. Without losing generality in our analysis, we set a heavier M_σ at 50 TeV (as the setup requires it to be quite heavy). At this stage, we would like to point out that the DM matter couples to σ through $S_1 - S_1 - \sigma$ interaction. This interaction can also help DM to annihilate into the SM particles through scalar mixing. Although these annihilations will have suppression coming from the mass of σ, they might still not be that small as these annihilations are also proportional to the $F_a \lambda_{S\eta}$. With $F_a = 10^{11}$ GeV and not so small value of $\lambda_{S\eta}$, the DM can still have significant annihilation cross-sections and such cross-sections might violate perturbative unitarity [95]. This demands $\lambda_{S\eta}$ to be extremely tiny. For simplicity, we set $\lambda_{S\eta} = 0$ throughout our analysis. Next, for the analysis purpose, we also define a mass-splitting, $\Delta M = M_{S_2} - M_{S_1}$ and consider it to be a free parameter rather than M_{S_2}. It is interesting to point out that once ΔM and F_a are fixed, the parameter ϵ_S automatically gets fixed, as can be seen from eq. (2.8). Before diving into the detailed analysis of the second DM candidate, we will like to mention the set of parameters that are relevant for the analysis of the DM phenomenology of the second DM candidate:

$$\{M_\Psi, M_{S_1}, \Delta M, F_a, \lambda_{SH}, f_i\}.$$

To demonstrate the above discussions, we display the variation of the relic density of S_1 with its mass in all the left panel plots of figure 2. In the right panel, we also exhibit the variation of the effective direct detection cross-section with M_{S_1} for different choices of parameters. In the top left panel of figure 2, we project the importance of the Yukawa coupling f_t while choosing fixed values of $\Delta M = 100$ GeV, $M_\Psi = 500$ GeV and $\lambda_{SH} = 0.01$. It is interesting to point out that for $\lambda_{SH} = 0.01$, the DM does not satisfy the correct relic density in a pure scalar singlet DM scenario. In these plots, we also set both Yukawa couplings $f_u = f_c = 0.01$ to highlight the importance of the top Yukawa coupling f_t for three values of f_t: 0.1 (blue), 0.5 (red) and 1.0 (green). Notice that for $f_t = 0.1$, with the increase in the DM mass, we first observe a resonance dip at $M_{S_1} = M_h/2$,[3] next, a fall is observed at $M_{S_1} = 80$ GeV where the annihilation of the DM to the $W^\pm$ boson opens up after which the relic density increases with the increase in the DM mass ($\langle \sigma v \rangle \propto 1/M_{S_1}$) and again drops at $M_{S_1} = 125$ GeV when the DM starts annihilating into the Higgs boson.[4] Finally, at a larger value of M_{S_1} ($M_{S_1} = 345$ GeV), when the mass difference between M_Ψ and M_{S_1} becomes relatively small, and the effect of DM co-annihilation with the VLQ comes into the picture, and a sharp drop in DM relic density is observed. In this region, although

[3] In a lower DM mass regime, DM annihilating to the three body final states $q\bar{q}g$ can also contribute significantly towards the relic density, where chirality suppression in the lower order process is lifted by final state radiation. We do not consider this three-body final state in our analysis as the entire low mass regime of the DM is already ruled out from the DD searches, as can be seen from the right panels of figure 2.

[4] We would also like to point out that for DM mass $M_{S_1} < M_t$, DM annihilations to gg (via a box diagram) [96, 97] or three-body final states like tWb [96] can also contribute towards the relic density of the DM for a significantly large Yukawa coupling f_t. We do not consider these processes in our analysis as we found that these processes remain suppressed for the choice of f_t we are interested in for our analysis.

JHEP12(2022)167

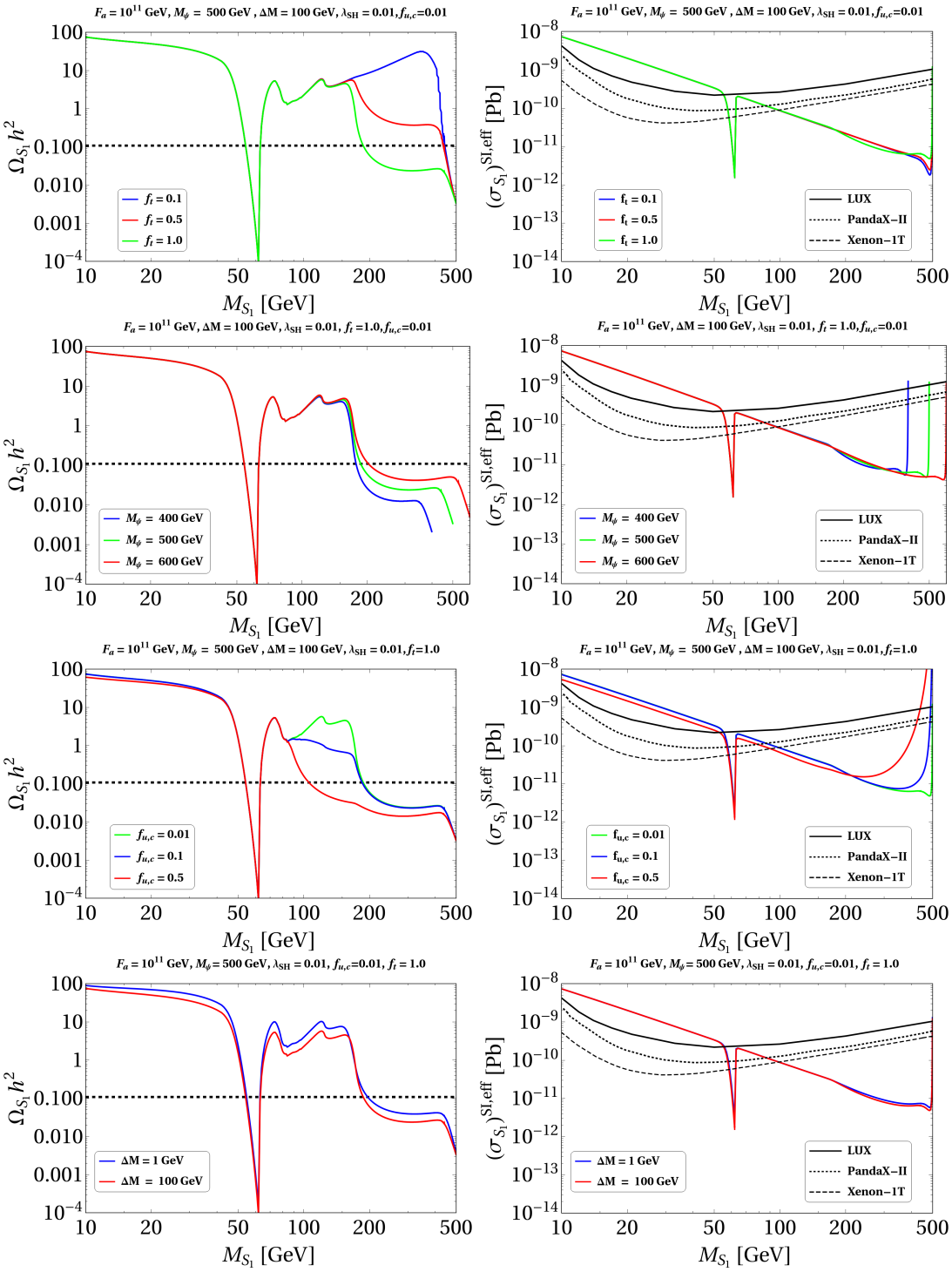

Figure 2. Variation of $\Omega_{S_1}h^2$ (left panel) and $\sigma^{\rm SI}_{S_{1,\rm eff}}$ (right panel) versus dark matter mass M_{S_1}. In all the plots we fix $F_a = 10^{11}$ GeV, $\lambda_{SH} = 0.01$. The Black dashed line in all the left plots corresponds to $0.120 - \Omega_a h^2$.

JHEP12(2022)167

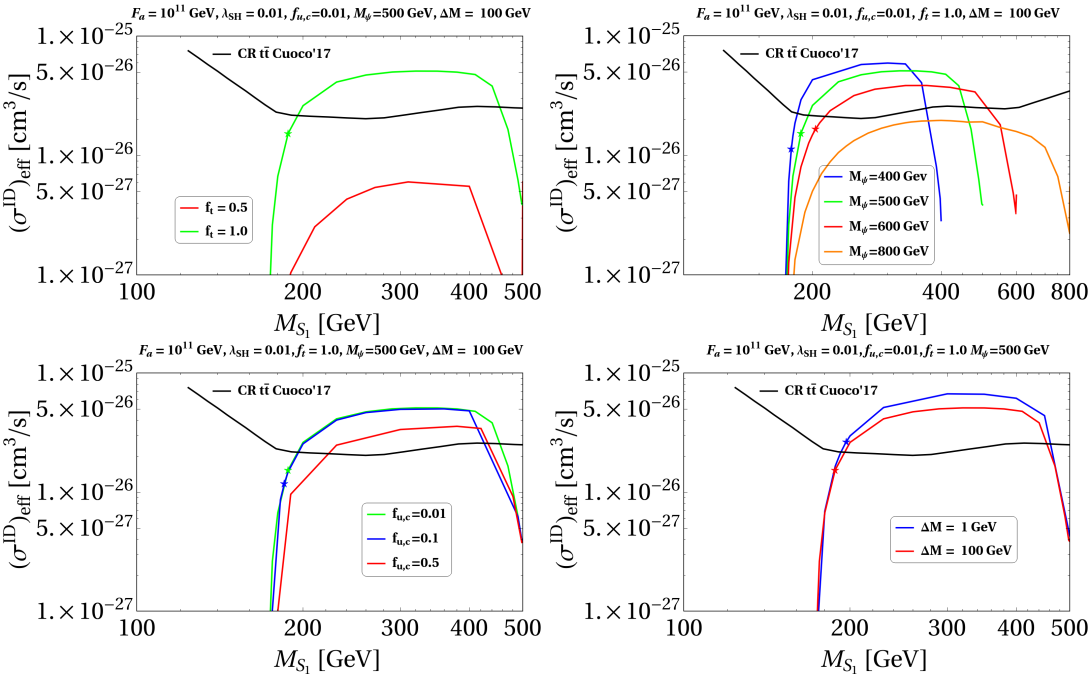

Figure 3. Variation of effective indirect detection cross-section versus DM mass. Variation for different values of f_t, the mass of VLQ, $f_{u,c}$, and ΔM are shown in top left, top right, bottom left and bottom right panels respectively. In all the plots we fix $F_a = 10^{11}$ GeV, $\lambda_{SH} = 0.01$. The solid black line shows the experimental upper bound in $t\bar{t}$ final state.

the DM co-annihilates with M_Ψ, the annihilation of Ψ with $\bar{\Psi}$ to the gluons dominates the effective annihilation cross-section (see eq. (4.4)) of the DM. Due to these co-annihilations, the relic density dark matter finally satisfies the condition $0.120 - \Omega_a h^2$ (denoted by the black dashed line) at $M_{S_1} = 444\,\text{GeV}$. Further increasing f_t to the higher values like 0.5 and 1.0, one notices that the DM annihilations to top quarks mediated by M_Ψ (see appendix A) start to dominate once the threshold of $M_{S_1} = M_{\text{top}}$ is crossed and the relic density can also satisfy the condition $0.120 - \Omega_a h^2$ near about $M_{S_1} \simeq 200\,\text{GeV}$ for $f_t = 1.0$. This figure illustrates the importance of VLQ in the DM phenomenology of the present setup as it makes huge parameter space allowed from the relic density, which was originally disallowed in the pure scalar singlet DM scenario.

In the top-right panel, we plot the spin-independent effective direct detection cross-section of S_1 with the DM mass and compare it with the experimental results. Notice that only the coupling f_u enters the direct detection cross-section of DM apart from the Higgs-portal coupling λ_{SH}. Note that the reduced values in the effective direct detection cross-section are the result of the rescaling in the two-component DM system (see eq. (4.8)). Additionally, Higgs resonance dip at $M_{S_1} = M_h/2$ and rise at $M_{S_1} \simeq 500\,\text{GeV}$ because of the interference among the direct detection diagrams (see appendix A). Here, one notices that the near resonance region remains discarded from the experimental bounds. Still, the other regions where relic density can be satisfied remain allowed from the direct detection searches.

JHEP12(2022)167

In the left panel of the second row in figure 2 we fix $f_t = 1.0$ and then study the effect of varying M_Ψ in $\Omega_{S_1}h^2 - M_{S_1}$ plane. As expected, the final fall in the relic density pattern happens at three different positions corresponding to the three different values of M_Ψ. With the heavier propagator mass i.e. $M_\Psi = 600\,\text{GeV}$, the effective annihilation cross-section of the DM to the top quark remains smaller in comparison to what is observed for $M_\Psi = 400\,\text{GeV}$ and hence relatively larger relic density is observed for $M_\Psi = 600\,\text{GeV}$ than for $M_\Psi = 400\,\text{GeV}$. Similarly, in the left panel of the third row, we depict the effect of varying f_u and f_c. For simplicity, here we also assume $f_u = f_c$. As expected, for a large value of $f_{u,c}$ the annihilation of DM to top and up (charm) quark final state also becomes dominant the moment the threshold $2M_{S_1} = M_{\text{top}} + M_{u(c)}$ is achieved. This leads to an increase in the DM annihilation cross-section, and consequently, a decrease in the relic density is observed. Next, in the left panel of the fourth row we show the effect of varying ΔM on the relic density of the DM. As expected, a smaller ΔM results in a larger effective DM annihilation cross-section and hence a smaller relic, so in order to satisfy the correct relic density a heavier DM mass is required. On the other hand, a larger ΔM requires a smaller DM mass to satisfy the observed relic density and hence the plot shifts towards the lower DM mass. Finally, the middle and bottom right panel of figure 2 can be followed from the one observed in the top right panel.

As can be seen from figure 2, the correct relic density is mostly satisfied in the parameter space where $M_{s_1} > M_t$. Hence, one needs to check the prospects of indirect detection of DM in our model specifically focusing on $t\bar{t}$ final states from the DM annihilations. We display our findings in figure 3 where we plot the effective indirect detection cross-section with DM mass and show the experimental upper bound (black solid line) of DM annihilating to $t\bar{t}$ final states that can be obtained from antiproton cosmic ray data [86]. In the top left panel of figure 3, we find that the DM mass for which the observed relic density satisfied (shown by green $\star$) in the top left panel of figure 2 is also allowed from the constraints coming from the indirect search bound. A similar situation is also observed in the top right and bottom left panels. On the other hand, in the bottom right panel where the variation with ΔM is studied, it found that a larger $\Delta M \sim 100\,\text{GeV}$ is prefered if one also considers the constraints coming from indirect search experiments. For this reason, we fix $\Delta M = 100\,\text{GeV}$ throughout our analysis.

In figure 4, we show the parameter space that remains consistent with the DM constraints and is also allowed by the constraints that come from the flavor observable like $D^0 - \bar{D}^0$ mixings in the bi-dimensional plane of $\Delta M_{\Psi S_1}/M_{S_1}$ Vs M_{S_1}, where $\Delta M_{\Psi S_1}$ is the mass difference between VLQ and DM, $M_\Psi - M_{S_1}$. Here, the dependence upon different Yukawa couplings ($f_u = f_c$ in the left panel and f_t in the right panel of the figure) is spotted with a continuous color map. Two discrete narrow slices at the top-left corner due to Higgs resonance. We are primarily interested in the non-resonant continuous region extended over vast parameter space. At the lower M_{S_1} end, this continuous region opens up when the DM pair annihilate into a top quark and up (charm) quark (see appendix A). Eventually, for a choice of heavier mass, the DM pair starts annihilating into the top pair.

This allowed region can be categorized into two distinct parts as upper and lower regions separated by a line where the mass difference between VLQ and DM equates to the top mass. Hence the upper region can be probed at the collider with on-shell production of

JHEP12(2022)167

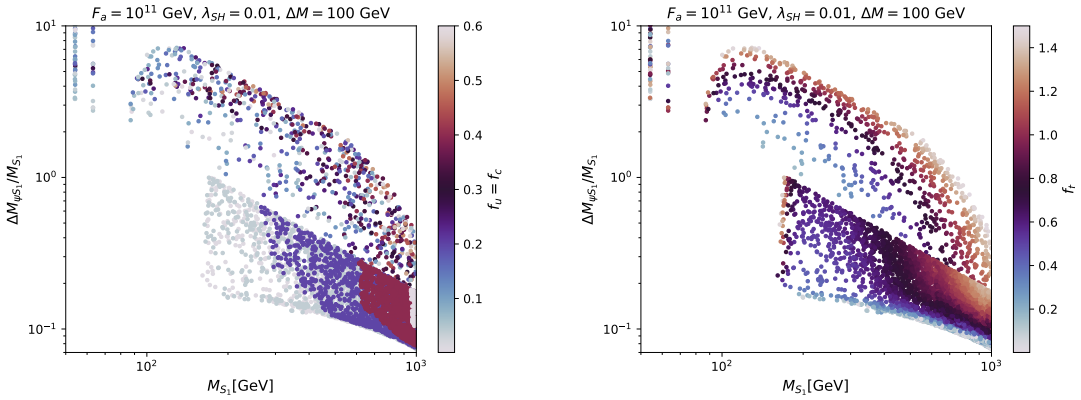

Figure 4. Parameter space satisfying observed DM abundance and also allowed by the direct search experiments in the bi-dimensional plane of $\frac{\Delta M_{\Psi S_1}}{M_{S_1}} - M_{S_1}$, where the colour coding is done with respect to: Left Panel: the Yukawa couplings $f_u = f_c$ and Right Panel: the Yukawa coupling f_t. In both the plots we fix $F_a = 10^{11}$ GeV, $\lambda_{SH} = 0.01$, $\Delta M = 100\,\text{GeV}$ while we vary f_t in the range 0–1.5 and $f_u = f_c$ in the range 0–1.5.

top quark from VLQ decay, while the lower region is sensitive to a probe with light quark search. We will further demonstrate in the next section how top quark searches from the boosted top jet can improve the search strategy in this region.

As a consequence of the narrow mass gap between scalar DM and VLQ, co-annihilation takes a leading role in most parts of the lower region. Precisely because of the same reason, this region is also susceptible to the direct detection probe. Variations of color contours for different f_u values are evident in the lower region of the left plot in figure 4. This reflects the gradually larger parameter space excluded due to direct detection constrain for a choice of larger f_u values. The lower value of mediator mass increases the direct detection cross-section. In order to keep this cross-section below the current direct detection bounds, a smaller f_u is required. On the contrary, the direct search experiments allow the upper region irrespective of the choice of f_u, and hence a uniform distribution of the colors is observed. This is because even for a large f_u, the DM-nucleon scattering cross-section still remains small due to the presence of a heavier mediator *i.e* M_Ψ.

At the right part of the same plot, one finds that with an increasing DM mass, a relatively smaller $\Delta M_{\Psi S_1}/M_{S_1}$ is required in order to satisfy the correct relic density, while the interplay between the DM mass, mediator's mass and the f_u makes these points allowed from the direct detection constraints. In this region, the DM dominantly annihilates into the top-quark pair and sub-dominantly into the top quark and up (charm) quark final states. Next, in the right panel of figure 4, we show the color coding with respect to f_t in order to highlight its significance. One observes the correct relic density in the top-left region of the plot due to the involvement of a large f_t as is also evident from the top left panel of figure 2. As expected for a lighter mediator mass, a relatively smaller f_t is required to satisfy the correct relic density, as is also observed while moving downward in the plot. Finally, the role of f_t becomes more prominent once the $M_{S_1} = M_{\text{top}}$ threshold is opened, as can also be seen from the right side of the plot.

JHEP12(2022)167

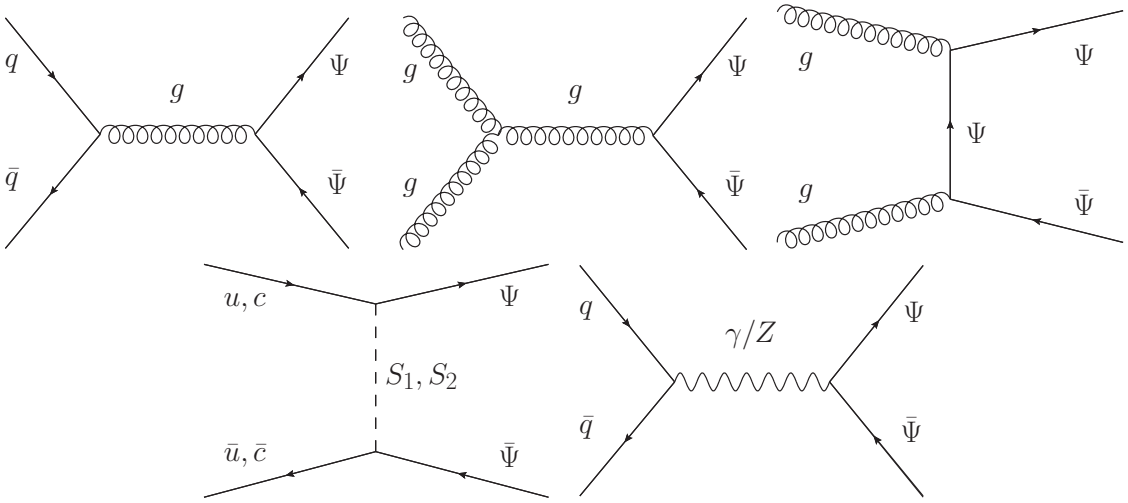

Figure 5. Representative Feynman diagrams for leading order partonic processes contributing VLQ pair production $pp \to \Psi\bar{\Psi}$ at LHC.

5 Collider analysis and results

The involvement of VLQ (Ψ) in the present setup opens up interesting collider prospects as they can be produced either in pair or associated with a scalar in the proton-proton collision at LHC. Among these production channels, $pp \to \Psi\bar{\Psi}$ and $pp \to \overset{(-)}{\Psi} S_{1,2}$, the cross-section of the second process strongly depends on the Yukawa coupling $f_{u,c}$, while the pair of VLQs is produced primarily by the strong interaction and hence model-independent. Once produced, the VLQ can decay preferably into scalar DM candidate or its heavier pair along with one of the up-type quarks as allowed kinematically. Hence primary LHC searches rely on identifying such quark jets along with missing transverse energy (MET or $\not{E}_T$) from DM production, as discussed in section 3.

It is noteworthy that a substantial parameter space exists in this model where the mass difference between VLQ and DM is significantly larger than the top quark mass while providing correct dark matter relic density and also allowed from the direct detection experiments. Here produced top quarks are expected to be fairly boosted by production from the decay of heavy mother (VLQ) particles. Such a prospect motivates us to look at this signal possessing a unique topology where hadronic decay of the top retains its collimated structure as a boosted fatjet[5] and is identified as a top-like-fatjet (J_t).

To probe these regions at the LHC, we consider pair production of VLQs and each of those further decay into the top quark associated with the scalar (DM or S_2). Here we adopt a significantly smaller Yukawas $f_u = f_c$ ($= 0.01$) so that the primary branching fraction of the decay of Ψ into the top quark is close to 100%. The signal topology is below, where we identify two final top fatjets associated with significant missing transverse

[5]We encountered a similar feature in the succession of different BSM scenarios [98–101], where boosted fatjet is probed in association with MET. Fatjets, in these searches, still harbor the intrinsic footprint of their root and manifest such features inside the jet substructure. Exploring this can provide additional tools to deal with a significant background involving QCD jets.

JHEP12(2022)167

Benchmark points	M_{S_1} (GeV)	$\Delta M_{\Psi S_1}$ (GeV)	ΔM (GeV)	f_t	$\Omega_{S_1}h^2$	$\sigma^{SI}_{S_1,\text{eff}}$ (pb)	$\sigma(pp \to \Psi\bar{\Psi})$ (fb)
BP1	301	305	100	0.8	0.108	9.24×10^{-12}	966
BP2	302	475	100	1	0.104	9.96×10^{-12}	223
BP3	403	405	100	1	0.109	5.77×10^{-12}	175
BP4	358	448	100	1	0.109	6.48×10^{-12}	177
BP5	433	364	100	1	0.107	4.6×10^{-12}	188
BP6	459	326	100	1	0.109	4.2×10^{-12}	208
BP7	494	273	100	1	0.107	3.79×10^{-12}	239
BP8	510	238	100	1	0.099	3.69×10^{-12}	278
BP9	527	224	200	1	0.103	3.56×10^{-12}	272
BP10	542	188	100	0.98	0.106	3.57×10^{-12}	321
BP11	678	349	100	1.3	0.109	2.14×10^{-12}	37

Table 2. Different benchmark points satisfy the observed relic density of DM, direct and indirect detection (not shown in the table) bounds, along with the constraints coming from the theoretical and LHC data, as listed in the text. M_{S_1} is the mass of the DM, S_1. f_t is the coupling strength of the interaction between top quark, VLQ, and the scalar S (see: eq. (2.1)). $\Delta M_{\Psi S_1} = M_\Psi - M_{S_1}$ and $\Delta M = M_{S_2} - M_{S_1}$. $\Omega_{S_1}h^2$ (see: eq. (4.7)) and $\sigma^{SI}_{S_1,\text{eff}}$ (see: eq. (4.8)) are the relic density of DM, S_1 and effective direct detection cross-section, respectively. Other parameters are $F_a = 10^{11}$ GeV, $\lambda_{SH} = 0.01$, and $f_u = f_c = 0.01$. The production cross-section of the partonic process $pp \to \Psi\bar{\Psi}$ at LO for different benchmark points before decaying into SM quark and scalar at 14 TeV LHC is given at the last column.

momentum from dark matter.

$$pp \to \Psi\bar{\Psi} \to (t, S_{1,2}), (\bar{t}, S_{1,2}) \equiv 2J_t + \not{E}_T \tag{5.1}$$

Note, S_2 can decay through two-body ($S_2 \to S_1 a$), three-body ($S_2 \to S_1\, j\, j$), and four-body ($S_2 \to S_1\, j\, b\, W$) decay modes, where suppressed multibody decay occurs through off-shell VLQ. Partonic level Feynman diagrams of the production of VLQ pair are shown in figure 5. Although the main contribution comes from the strong interaction, we keep all the diagrams for completeness. Few representative benchmark points (BPs) are listed in table 2; those provide observed relic density of DM and allowed from the direct and indirect detection experiments along the constraints coming from the theoretical and LHC data as listed in section 3. Also, the production cross-section of the partonic process $pp \to \Psi\bar{\Psi}$ at LO for different benchmark points before decaying into SM quark and scalar at 14 TeV LHC is shown at the last column table 2. For our analysis, we have used an NLO QCD K-factor of 1.33 for the $pp \to \Psi\bar{\Psi}$ production.[6]

[6]We estimate an approximate NLO (QCD) K-factor for the process $pp \to \Psi\bar{\Psi}$ by replacing Ψ with the top quark of mass m_Ψ at the MadGraph5_aMC@NLO and took the most conservative value over this mass range.

JHEP12(2022)167

5.1 Simulation details with signal and backgrounds

In preparation for our investigation of this Hybrid KSVZ framework through VLQ pair production at the LHC, we require a realistic setup to simulate both the signal processes as well as a careful selection of background processes that can mimic the signal.

We implement this Hybrid KSVZ framework in FeynRules [88] to generate the UFO model file required for matrix element generation for Monte-Carlo event generator. Parton level events are generated in the MadGraph5_aMC@NLO environment [102] and further pass through Pythia8 [103, 104] for showering, fragmentation and hadronization. Background events are generated along with two to four additional jets MLM matching [105, 106] with virtually-ordered Pythia showers to avoid any double counting. We include higher-order corrections for different processes by multiplying the appropriate K factor. An in-built NN23LO1 pdf set is adopted for the parton distribution functions (PDF), and a default dynamical factorization scale is used for events generation. The showered events are further passed through Delphes3 [107] to include detector effects with the default CMS card. Jets (j) of radius parameter 0.5 are constructed with the anti-k$_T$ [108] clustering algorithm, where we used the particle-flow towers and particle-flow tracks as input. We implement the Cambridge-Achen (CA) [109] algorithm to construct large radius fatjets – J. Fastjet 3.2.2 [110] is used for clustering fatjets of radius parameter $R = 1.5$. A boosted top gives a fatjet whose radius parameter is approximately govorned by $R \sim 2m_t/P_T$, where m_t (P_T) is the mass (transverse momentum) of the top quark. Hence, the minimum transverse momentum required by each top to form such a fatjet is $P_T \gtrsim 200\,\text{GeV}$. Finaly, we implement the adaptive Boosted Decision Tree (BDT) algorithm to perform the multivariate analysis (MVA) in the TMVA [111] framework.

Our analysis considers all the backgrounds that significantly contribute to the two boosted top fatjets with large missing transverse momentum, as listed below.

$t\bar{t}$+ jets. Top pair production with the semi-leptonic top decays is the most dominant background for our signal process. Although pure hadronic decay of tops can offer two boosted top jets, the requirement of a considerable amount of missing energy reduces this background by a significant factor of 100, where mismeasurement of hadronic activities acts as a source of MET. In the semileptonic decay, one top decay hadronically and is reconstructed as boosted top jet, and the other top decay leptonically gives a significant amount of missing energy when the lepton escapes detection. Other boosted jet comes from the QCD radiation. This background is matched with the MLM matching scheme up to two extra jets.

QCD background. QCD background is enormous at the LHC but can be reduced to a negligible contribution (see, for example, ref. [112]). Even after the requirements of two boosted fatjets, we are left with a remarkably large number of events from this background. We further require at least one b tag within the leading or sub-leading fatjet. Contribute negligibly after additional suppression of 100 comes from fake MET from hardons and another 50 from the requirement of b tag fatjet. We do not include this background in our analysis.

JHEP12(2022)167

***tW*+ jets.** Single top production associated with W boson significantly contributes to the SM background. The top is reconstructed as the boosted top where the b quark is tagged within it, and the W boson decays leptonically to give rise to missing transverse momentum. In contrast, another boosted fatjet arises from QCD jets. MLM matching up to two extra jets is done for this process.

***V*+ jets.** (Simi-)invisible decay of W/Z vector boson in addition to QCD radiation that emulates the fatjet can contribute sizably even with a requirement of sizeable reconstructed mass of the fatjet. We do MLM matching up to four extra jets for both processes. A generation level cut $\not{E}_T > 100\,\text{GeV}$ is applied for both processes to obtain statistically significant background events.

di-boson + jets. Minor contribution can come from Di-boson + jets. We retain all the three di-boson background processes ($pp \to WZ,\ WW,\ ZZ$) in our analysis. Among the three, WZ + jets contribute the most. All three processes are matched up to two extra jets with an MLM matching scheme. In all the cases, one of the vector boson decay invisibly ($Z \to \nu\nu$) or leptonically ($W \to l\nu$) to give $\not{E}_T$. One of the boosted fatjet comes from QCD jets, and another fatjet comes from either hadronically decaying vector boson or the QCD jets.

***ttV*.** Such processes have three body phase spaces and have less cross-section than other background processes mentioned above. Both the tops can be reconstructed as boosted fatjets, while $\not{E}_T$ comes from the invisible or leptonically decay of the Z and W boson, respectively. Among these two, $t\bar{t}Z$ contributes the most because of the larger cross-section and more significant efficiency when applying $\not{E}_T$.

We consider all contributions generating those events at leading order and normalize with the NLO (QCD) cross-section. Higher-order QCD corrected production cross-section at the 14 TeV LHC for different background processes accounted in this analysis are listed in table 3.

5.2 Construction of high-level variables and cut-based analysis

Once we have generated our signal and background processes after the realistic detector-level simulation, the next task is constructing high-level event variables sensitive to kinematic configuration signal and background processes. For example, the unique point of this collider study counts on the fatjet characteristic and its different properties related to the mass-energy distribution within these fatjets. We categorize some of the useful variables for our analysis in the following bulleted points:

N-subjettiness ratio. In the case of a highly boosted top quark, one can capture all three hadronically decayed constituents of the top quark within a single large-radius jet (fatjet). The whole energy of a reconstructed top-fatjet is distributed around three subjet axes. Assuming N number of subjets belong to the fatjet, N-subjettiness is defined by the angular distance in the transverse plane of constituents of the fatjet from the nearest subjet

JHEP12(2022)167

Background		σ (pb)
top pair [113]	$t\bar{t}$+ jets	988.57 [N^3LO]
single top [114]	tW	83.1 [N^2LO]
mono-V boson [115, 116]	Z+ jets	6.33×10^4 [N^2LO]
	W+ jets	1.95×10^5 [NLO]
di boson [117]	ZZ+ jets	17.72 [NLO]
	WW+ jets	124.31 [NLO]
	WZ+ jets	51.82 [NLO]
mono-V + $t\bar{t}$	$t\bar{t}Z$	0.911 [NLO]
	$t\bar{t}W^{\pm}$	0.636 [NLO]

Table 3. Higher-order QCD corrected cross-section at the 14 TeV LHC of different background processes considered in our study. The order of QCD correction is given in brackets. For the final process, higher-order QCD corrected cross-section in five massless quark flavors at 14 TeV LHC obtained from MG5_aMC@NLO. Default factorization and renormalization scales and an in-built NN23NLO pdf set are used.

axis and weighted by the transverse momentum of the constituents as below [118, 119]:

$$\tau_N = \frac{1}{\mathcal{N}_0} \sum_i P_{T,i} \min\{\Delta R_{i,1}, \Delta R_{i,2}, \ldots, \Delta R_{i,N}\}. \tag{5.2}$$

Here, the summation goes over all the particles inside the jet. The denominator is $\mathcal{N}_0 = \sum_i P_{T,i} R$, where $P_{T,i}$ and R are the transverse momentum of the i-th constituent and radius of the jet, respectively. Since N-subjettiness determines the jet shape, the N-subjettiness ratios, such as τ_{31} and τ_{32} are good observables in signal background analysis. τ_{32} effectively distinguishes the top signal from two-prong fatjets arising from the boosted W or Z boson in the background. In contrast, τ_{31} is also effective for separating the top signal from the one-prong QCD fatjets that contribute significantly to the background.

Pruned jet mass. Jet-mass is a good variable for classifying a boosted top-fatjet from the two-prong fatjets from the boosted W/Z boson or one-prong QCD fatjets. The jet mass, $M_J = (\sum_{i \in J} P_i)^2$, where four-momentum of i-th energy hit in the calorimeter is P_i. Since large radius jets pick additional soft contributions from underlying QCD radiations, we must remove these soft and wide-angle radiations for more realistic predictions. Different jet grooming techniques, pruning, filtering, and trimming [120–123] are available to remove those softer and wider angle radiations while we consider pruning in our analysis. In the first step of pruning, we define fatjet using the CA algorithm, and in the second step, we pruned its constituents in each recombination step.

$$Z = \min(P_{Ti}, P_{Tj})/P_{T(i+j)} < Z_{\text{cut}} \qquad \text{and} \qquad \Delta R_{ij} > R_{\text{fact}} \,. \tag{5.3}$$

The merging $i, j \to J$ is vetoed when both the conditions are satisfied. Pruning is parametrized by two parameters, the softness parameter, Z, and the angular distance

JHEP12(2022)167

of the constituents, ΔR_{ij}. We chose $Z_{\rm cut} = 0.1$ [122] and $R_{\rm fact} = 0.86$ ($\sim m_t/P_{T,\rm top}$) [123] in our analysis.

Primary event selection criteria. Based on our previous discussion and construction of high-level variables, we identify two large-radius jets, leptons, and missing transverse energy as per the following event selection criteria both for the signal and background events alike:

1. Each event should contain at least two fatjets constructed by CA algorithm with radius parameter $R = 1.5$, and each of them has transverse momentum, $P_T(J_0), P_T(J_1) > 200\,\text{GeV}$. Here, J_0 and J_1 represent the leading and subleading fatjet.

2. Each event is selected with a minimum missing transverse energy $\not{E}_T > 100\,\text{GeV}$.

3. Since our signal does not contain lepton, we veto any event if it contains any lepton with transverse momentum, $P_T(l) > 10\,\text{GeV}$ within pseudorapidity $|\eta(l)| < 2.4$.

4. To minimize jet mismeasurement contribution to $\not{E}_T$, we keep an azimuthal separation between each fatjet and $\not{E}_T$, $|\Delta\Phi(J_{0,1}, \not{E}_T)| > 0.2$.

The normalized distribution of different observables of a sample signal benchmark point, BP3, and bin-wise stacked histogram of all the backgrounds are shown in figure 6. These plots are shown after demanding at least one the b tag within leading or subleading fatjet, enhanced $\not{E}_T > 150\,\text{GeV}$, over the preselection cuts already described for 14 TeV LHC.

The prime background $t\bar{t}+$ jets, where one of the top decay hadronically and the other decays leptonically, is shown by the top most blue shade, while the solid red line indicates the sample signal, BP3. The distributions of the pruned jet mass of the leading (M_{J_0}) and subleading (M_{J_1}) fatjets are given in figure 6a and figure 6b, respectively. At LO, Ψ and $\bar{\Psi}$ produce back to back, each one followed by decay into an (anti)top quark and $S_{1,2}$. In most events in this benchmark point, these tops are boosted as they are produced from the decay of heavy particles. When the top is sufficiently boosted, all three constituents of the top quark fall within a single large-radius jet, giving a three-prong jet substructure and pruned jet mass very close to the top quark mass. For the signal, we get a sharp peak around the top quark mass for both the leading and subleading fatjet. These large radius jets sometimes misses some of the constituent sub-jets, especially when the boost of the top quark is relatively low, causing a secondary peak near the W/Z boson mass for both the fatjets of the signal. For semi-leptonic $t\bar{t}+$ jets background, the top which decays hadronically gives the leading fatjet for a significant number of events and causes a sharp peak near top mass in the leading fatjet mass distribution. From the demand for a very high missing transverse momentum, $t\bar{t}+$ background contributes to a phase space region where the b-jet from the leptonically decaying top quark generates the subleading fatjet predominantly. Consequently, subleading fatjet mass generates its peak near 20 GeV from QCD radiation.

The total missing transverse energy distribution is shown as another interesting variable in figure 6j. In the case of signal, we have two missing DM particles coming from the decay

JHEP12(2022)167

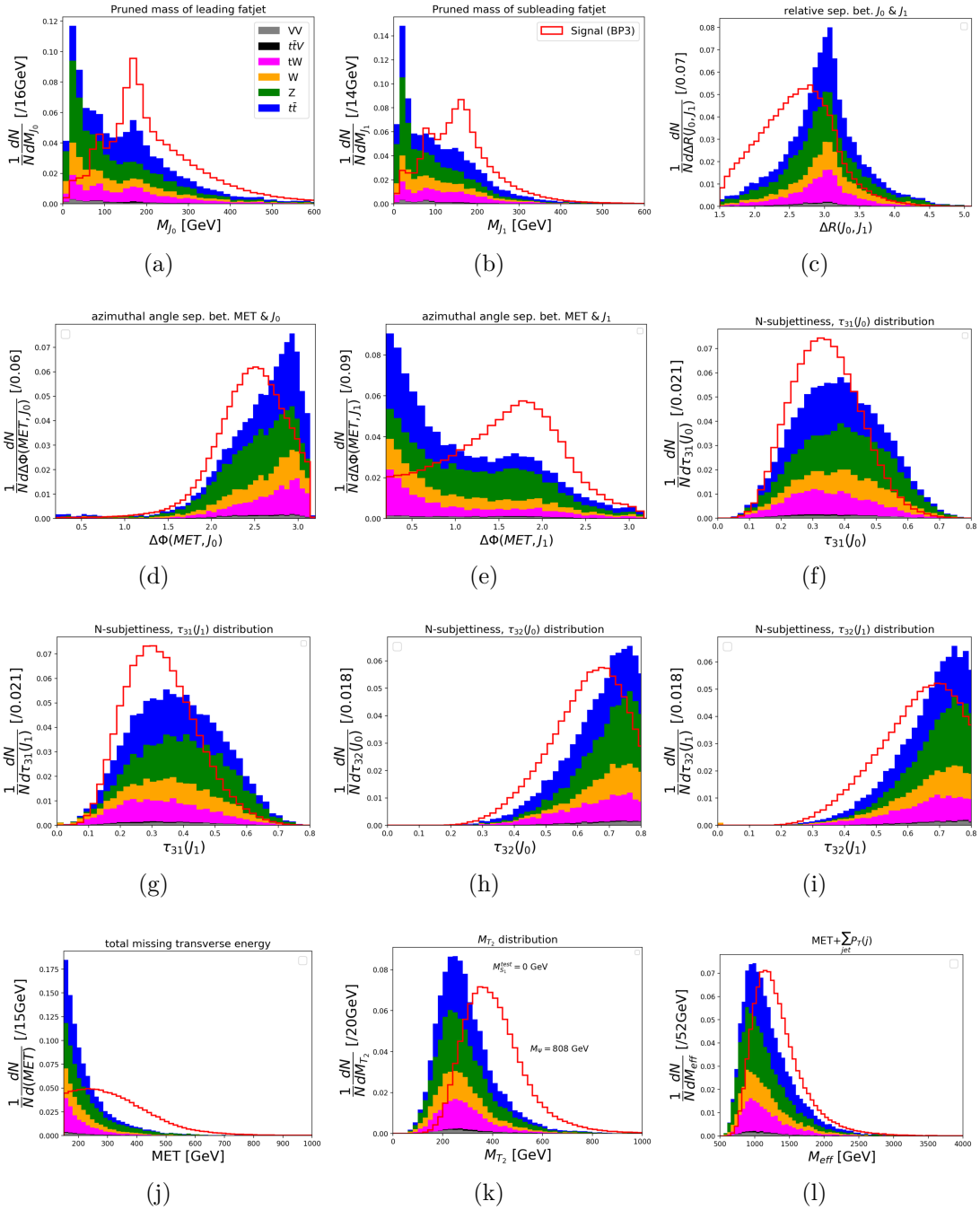

Figure 6. Distributions of different kinematical variables for the signal (BP3) and all the backgrounds contributing to the fatjets $+\not{E}_T$ final state after imposing the b tag within leading or subleading fatjet, $\not{E}_T > 150\,\text{GeV}$, and the primary event selection criteria (described in the text) for 14 TeV LHC. The normalized distribution for the signal is given by the solid red line. The events of each background process have been weighted by their cross-section and the cut efficiency after applying the previously mentioned cuts. Each background process is then normalized to the sum of individual cross-section times cut efficiency. Colors show the contribution of the individual background process.

JHEP12(2022)167

	BP3	$t\bar{t}$**+jets**	tW**+jets**	ttZ	ttW	Z**+jets**	W**+jets**	WZ**+j**	ZZ**+j**	WW**+j**
C1	5969 [100%]	9.6×10^4 [100%]	5.1×10^4 [100%]	1048 [100%]	111 [100%]	3.5×10^5 [100%]	1.9×10^5 [100%]	1.3×10^4 [100%]	1.6×10^3 [100%]	3.6×10^3 [100%]
C2	5296 [88.73%]	4.2×10^4 [43.89%]	2.12×10^4 [41.96%]	793 [75.71%]	64 [57.53%]	2.28×10^5 [65.06%]	1.06×10^5 [53.78%]	8.11×10^3 [64.34%]	969.2 [61.73%]	1.6×10^3 [43.97%]
C3	4424 [74.11%]	3.21×10^4 [33.60%]	1.59×10^4 [31.42%]	656 [62.63%]	54.1 [48.73%]	3.36×10^4 [9.57%]	1.64×10^4 [8.32%]	1.5×10^3 [11.89%]	267 [17.0%]	341.1 [9.37%]
C4	1005 [16.85%]	4.02×10^3 [4.20%]	1.72×10^3 [3.39%]	185 [17.66%]	16.7 [15.07%]	1.54×10^3 [0.44%]	926 [0.47%]	72 [0.57%]	10.4 [0.66%]	26 [0.71%]
C5	666 [11.16%]	2.46×10^3 [2.57%]	1.07×10^3 [2.12%]	132.5 [12.64%]	12 [10.84%]	842 [0.24%]	493 [0.25%]	42.5 [0.337%]	7.1 [0.45%]	15.7 [0.43%]
C6	432 [7.24%]	411 [0.43%]	197 [0.39%]	54 [5.12%]	3.1 [2.78%]	260 [0.074%]	132 [0.067%]	17.5 [0.139%]	4.3 [0.272%]	1.7 [0.047%]

Table 4. The cut efficiency and expected number of events after the corresponding cuts for the signal and all the backgrounds contribute to the fatjets $+\not{E}_T$ final state at the 14 TeV LHC and 139 fb^{-1} integrated luminosity. The effectiveness of different selection cuts can be followed in the form a cut flow from top to bottom after applying (C1) Preselection cuts, (C2) $\not{E}_T > 150$ GeV, (C3) requiring at least one b-tag within J_0 or J_1, (C4) 120 GeV$< M_{J_0}, M_{J_1} < 230$ GeV, (C5) $\tau_{31}(J_0), \tau_{31}(J_1) < 0.4$ and finally, (C6) $M_{T_2} > 320$ GeV. A sample benchmark point, BP3, is presented in this table.

of Ψ pair, where they primarily produce back to back, so the $\not{E}_T$ has uniform distribution as two missing particles can avail entire phase space. In contrast, the background drops sharply for large $\not{E}_T$. Distributions of the azimuthal separation of the leading and subleading fatjets from the $\not{E}_T$ are presented in figure 6d and figure 6e, respectively. As stated earlier, two missing particles can avail the entire phase space for the signal, so both $\Delta\Phi(MET, J_{0,1})$ have a uniform distribution. For a significant amount of events of the $t\bar{t}$+ jets background, the b-jet from the leptonically decaying top quark behaves as a subleading fatjet (J_1), and the neutrino gives the $\not{E}_T$, where we select the events that have large $\not{E}_T$. Hence, the azimuthal separation of J_1 from $\not{E}_T$ gets a maximum at a lower value. In contrast, the azimuthal separation of the leading fatjet (J_0) from $\not{E}_T$ peaks near $\sim \pi$ rad. The distribution of $\Delta R(J_0, J_1)$, angular distance between J_0 and J_1 in the transverse plane is given in figure 6c.

The distribution of the kinematic variable τ_{31} for both leading and subleading fatjet are shown in figure 6f, figure 6g, respectively. In both distributions, as expected, the signal has a peak for a smaller value of τ_{31} representing that signal fatjets have a three-prong structure. Similarly, the distribution of the kinematic variable τ_{32}, which separates the three-prong fatjet from the two-prong fatjet, are presented in figure 6h, figure 6i. $\tau_{32}(J_0)$ has a peak near 0.6 and 0.75 for signal and background, respectively. Note that we do not apply any mass window in generating these distributions, but if we do, the peaks of τ_{32} move towards a lower value. So, in the final event selection in the cut-based analysis, we apply a mass window to discriminate the signal from the background better.

The distribution of kinematic stransverse mass variable M_{T2} [124–126] is given in figure 6k. Assuming DM mass is unknown to us, we construct M_{T2} after setting trial DM

JHEP12(2022)167

BP	BP1	BP2	BP3	BP4	BP5	BP6	BP7	BP8	BP9	BP10	BP11
σ	11.4	12.8	11.1	9.9	6.9	5.3	4.0	3.6	2.5	1.2	2.8
$\frac{S}{B}$	0.41	0.47	0.40	0.35	0.23	0.17	0.13	0.12	0.08	0.04	0.09

Table 5. Statistical significance (σ) and the signal-to-background ratio ($\frac{S}{B}$) are shown for the signal corresponding to different benchmark points contributing to the fatjets $+\not{E}_T$ final state at 14 TeV LHC and 139 fb^{-1} integrated luminosity.

mass as zero in this construction. SM particles have a smaller mass compared to the mass of Ψ, so the M_{T2} distribution of signal and background are well separated. Since we do not want to find the correct mass of the mother particle (Ψ), this variable is used to discriminate the signal from the background efficiently. The distribution of $M_{\rm eff}$ is given in figure 6l. Effective mass is defined as

$$M_{\rm eff} = \not{E}_T + H_T, \tag{5.4}$$

where $H_T \equiv \sum_{i=1}^{N_J} P_{iT}$ (N_J is the number of visible jets) is the scalar sum of the transverse momentum of the jets. The above distributions show that all the variables are very good at distinguishing the signal from the background.

We apply the following selection cuts to demonstrate a cut-based analysis (CBA) over the preselection cuts (described before) to increase the signal-to-background ratio. Note that our final results are based on sophisticated multivariate analysis with improved statistics. So, the next part is for demonstration purposes without putting much effort into optimizing all the selection criteria. Here, we offer a cut-flow in cut-based analysis to better understand the signal and background differential distributions.

Final selection cuts:

5. We increase $\not{E}_T$ from 100 GeV to 150 GeV since it reduces the background sharply than the signal.

6. Demand an additional b-tag withing either leading or subleading fatjet is applied. The b-tag efficiency for the signal within leading or subleading fatjet is 84%. This requirement reduces $Z+$ jets and $W+$ jets backgrounds substantially below $t\bar{t}+$ jets background.

7. We select the events for which the pruned mass of the leading and subleading fatjets falls within 120 GeV$< M(J_0), M(J_1) <$ 230 GeV.[7] The lower threshold helps us reduce different backgrounds where one or both the fatjets originated from QCD radiation or W/Z boson.

[7]Note that, in the MVA next section, we retain only the lower mass threshold and let the framework select the non-linear cuts to get the optimal signal-to-background ratio.

JHEP12(2022)167

Signal	BP1	BP2	BP3	BP4	BP5	BP6	BP7	BP8	BP9	BP10	BP11
	6625	3525	2341	2711	2176	1924	1424	1081	915	552	385

SM BG	tt+jets	tW+jets	ttZ	ttW	Z+jets	W+jets	WZ+jets	ZZ+jets	WW+jets
	8928.06	3815.42	294.35	25.93	3527.96	2408.37	172.35	27.54	46.49

Table 6. The expected number of signal and SM background events after applying $M_{J_0} > 120\,\text{GeV}$, $M_{J_1} > 120\,\text{GeV}$ and b-tag (within leading or subleading fatjet), $\not{E}_T > 150\,\text{GeV}$ in addition to preselection cuts at 14 TeV LHC for 139 fb^{-1} integrated luminosity.

8. To discriminate further the fatjets from QCD jets, we use N-subjettines and collect the events that satisfy $\tau_{31}(J_0)$ and $\tau_{31}(J_1) < 0.4$.[8]

9. We impose $M_{T_2} > 320\,\text{GeV}$. This requirement increases the signal-to-background ratio ($\frac{S}{B}$). For example, in the case of BP3, $\frac{S}{B}$ changes from 0.13 to 0.4 (table 4).

The expected number of signal (for a sample benchmark point, BP3) and background events and cut efficiency after imposing the preselection cuts and final selection cuts at 14 TeV LHC for 139 fb^{-1} integrated luminosity are shown in table 4. Statistical significance and the signal-to-background ratio for different benchmark points are shown in table 5. $\sigma = \frac{N_S}{\sqrt{N_S+N_B}}$ defines the statistical significance, where N_S and N_B are the expected signal and background events after the cuts, respectively. The statistical significance for the signal of different benchmark points is above the discovery potential for an integrated luminosity of 139 fb^{-1}. We also have good statistics indicating that extracting the VLQ pair from the Standard Model background is not tough.

5.3 Analysis based on the multivariate gradient boosting technique

In the previous section, we constructed high-level variables and demonstrated their potential in a CBA. This section extends that idea to perform a more sophisticated MVA. In these analyses, MVA generally gives better sensitivity than CBA if appropriate kinematic variables are utilized, where we may get significance above the discovery limit for the benchmark points that is unable through CBA. The M_{J_0} and M_{J_1} distribution (figure 6a, figure 6b) have the largest peak around the top mass, and the signal is much harder than the background for $M_{J_{0,1}} > 120\,\text{GeV}$. Instead of both lower and upper mass thresholds to set an allowed window, we retain only a lower mass threshold of 120 GeV for both the fatjets for event selection in MVA for a higher number of events. We expect the MVA framework to select nonlinear variable space to get the optimal signal-to-background ratio. The 120 GeV cut on both fatjets reduces the backgrounds drastically compared to the signal for which fatjets arrises from the QCD jet (one-prong) or boosted W/Z boson (two-prong). We also demand at least one b tag within the leading or subleading fatjet for event selection in MVA, reducing the background much more than the signal. From the missing energy

[8] One may use the N-subjettiness variables $\tau_{32}(J_0)$ and $\tau_{32}(J_1)$ to discriminate the fatjets from two-prong fatjets originated from boosted W/Z bosons. Since we analyze the same signal using MVA in the next section, we do not check τ_{32} variables in CBA.

JHEP12(2022)167

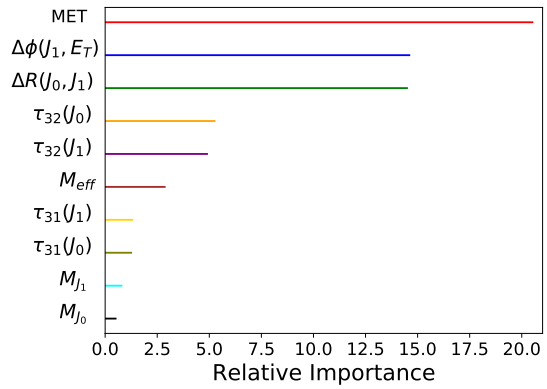

Figure 7. Relative importance (Method unspecific) of the different kinematic variables used in MVA. We get those numbers for BP3 from the TMVA package. Those numbers can change a little bit if one chooses a different algorithm.

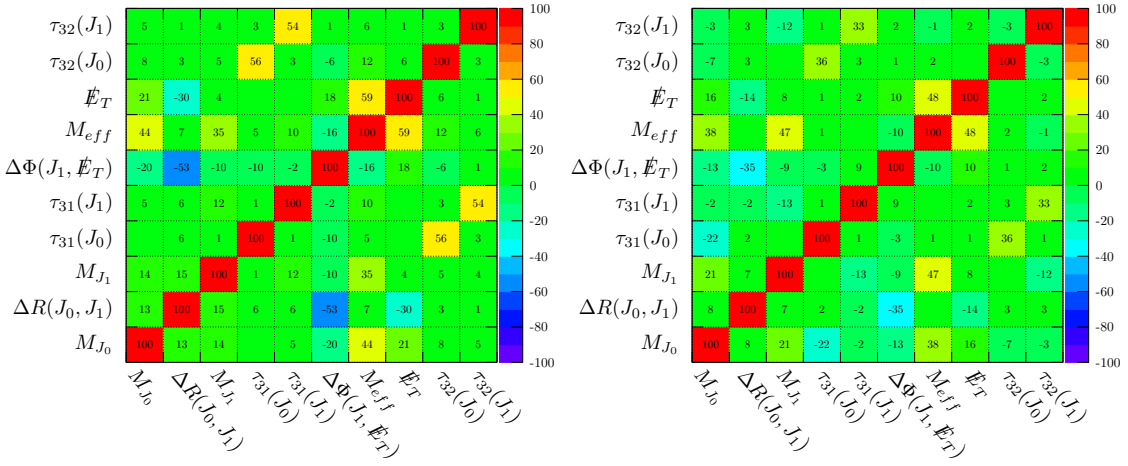

Figure 8. Linear correlation coefficients (in percentage) between different kinematical variables for the signal (BP3, left panel) and background (right panel). Missing entries correspond to a negligible correlation smaller than one. Positive and negative coefficients indicate that two variables are correlated or anti-correlated, respectively.

distribution (figure 6j), we see most background events exist in low missing energy, so after demanding large missing energy, we reduce the background significantly compared to the signal. So we apply $\not{E}_T > 150\,\text{GeV}$ for the event selection in MVA.

With these selection criteria, we keep all other variables unrestrained, giving enough scope to the multivariate analysis to find an optimal nonlinear cut based on the suitable variables. The expected number of signal and background events after applying MVA selection cuts at 14 TeV LHC for 139 fb^{-1} integrated luminosity is given in table 6. We apply the adaptive Boosted Decision Tree (BDT) algorithm in our analysis and construct statistically independent signal and background event samples. Each event sample is split

JHEP12(2022)167

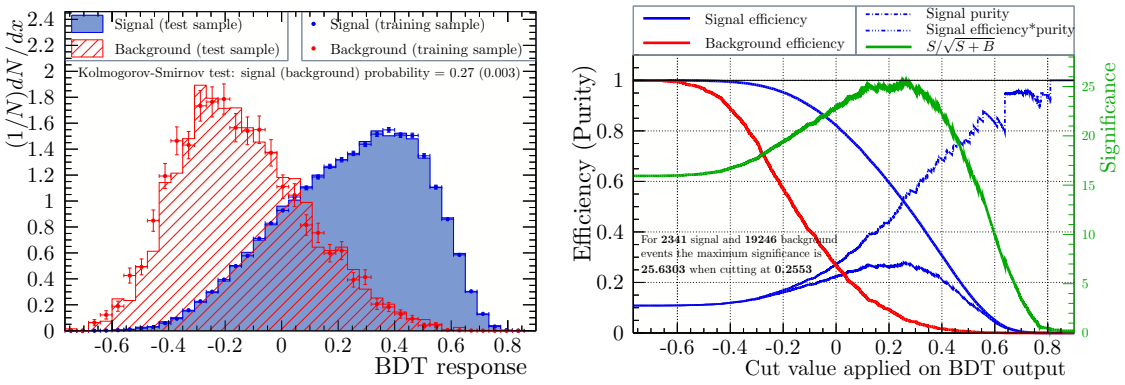

Figure 9. Left panel: normalized distribution of the BDT response for both signal (blue, BP3) and background (red) classes (both training and testing samples of both classes). Right panel: signal (blue) and background (red) efficiencies and the statistical significance of the signal (green) as a function of cut applied on BDT output.

randomly for training and testing purposes. Since multiple processes contribute to the total background, we generate them with two to four extra jets MLM matching separately and combine them in proportion to their proper weight to get a combined background sample. For multivariate analysis, a final set of kinematic variables are accepted from a larger set, where we retain only those variables that are less (anti) correlated in both signal and background and have larger relative importance. Even before implementing any model, a variable can have more relative importance than another when it has larger discriminating power separating the signal class from the background class. We find $P_T(J_0)$, $P_T(J_1)$, and $\sqrt{\hat{S}_{\rm min}}$ [127, 128] are highly correlated with $M_{\rm eff}$ in both signal and background. However, we keep $M_{\rm eff}$ as it has larger relative importance than other variables. $\sqrt{\hat{S}_{\rm min}}$ is defined as

$$\sqrt{\hat{S}_{\rm min}} = \sqrt{\left(\sum_j E_j\right)^2 - \left(\sum_j P_{z,j}\right)^2} + \not{E}_T \tag{5.5}$$

where summation runs over all the visible jets. From eq. (5.4) and eq. (5.5), the above correlations are expected. We also observe that $\Delta\Phi(J_0, \not{E}_T)$ and $\Delta\Phi(J_1, \not{E}_T)$ are moderately anti-correlated in signal but highly anti-correlated in background. The moderate anti-correlation of the signal is because of the total availability of phase space of the two missing particles. In the case of background, for example, the principle $t\bar{t}$+ jets background, the only allowed phase space is when both top and anti-top are highly boosted and move almost in the opposite direction, where one of the reconstructed tops gives the leading fatjet, and another one gives both subleading fatjet and large missing transverse momentum. As a result, these two variables are highly anti-correlated in the background. We keep $\Delta\Phi(J_1, \not{E}_T)$ as it has larger relative importance than $\Delta\Phi(J_0, \not{E}_T)$. We notice that M_{T2} and $\not{E}_T$ are also highly correlated in signal and moderately in background. Since $\not{E}_T$ has the largest relative importance, we choose $\not{E}_T$ over M_{T2} for MVA analysis. The relative

JHEP12(2022)167

importance of the different kinematic variables used in MVA is presented in figure 7 for sample benchmark point BP3. From the normalized distributions in the previous section, we notice that all variables used in MVA are outstanding in distinguishing the signal from the background. However, the $\not{E}_T$, $\Delta R(J_0, J_1)$, and $\Delta\Phi(J_1, \not{E}_T)$ are the finest among all these useful variables. The linear correlation coefficients (in percentage) between different kinematical variables for the signal (BP3, left panel) and background (right panel) is presented in figure 8. BDT algorithm may lead to overtraining for wrong choices of different (BDT specific) parameters during training. Such overtraining can be avoided if one checks the Kolmogorov-Smirnov probability during training. We train the algorithm separately for every benchmark point and confirm that no overtraining exists in our analysis.

The normalized distribution of the BDT response of the signal (BP3) and the background classes (both training and testing samples of both classes) is shown in figure 9. We notice both the classes are well separated. We present the variation of the signal and background efficiencies and the statistical significance of the signal (BP3) with the cut applied on the BDT response in the right panel of figure 9. Statistical significance is defined as $\sigma = \frac{N_S}{\sqrt{N_S+N_B}}$. The number of events that survive after applying the $\mathrm{BDT_{res}} > \mathrm{BDT_{opt}}$ cut for signal and background is N_S and N_B, respectively. $\mathrm{BDT_{opt}}$ is the optimal cut for which the significance is maximum. In table 7 (upper) N_S, N_B, σ, and $\frac{N_S}{N_B}$ are presented for different benchmark points at 14 TeV LHC with integrated luminosity 139 fb^{-1}. We find that for a few of the chosen BPs, the number of signal events is larger than the background events after the $\mathrm{BDT_{res}} > \mathrm{BDT_{opt}}$ cut, and for all eleven benchmark points, we reach the discovery potential with integrated luminosity 139 fb^{-1}.

Our next interest would be to verify how significance varies with the mass of the scalar S_2. For that purpose, we generated the event samples separately for different masses of the S_2 with the same DM mass $M_{S_1} = 403\,\mathrm{GeV}$, VLQ mass $M_\Psi = 808\,\mathrm{GeV}$, and the coupling constant $f_t = 1$. We train the algorithm separately for different samples of different S_2 masses and confirm that no overtraining exists in our analysis and perform the MVA.

There are two possible hierarchies possible: $M_{S_2} > M_\Psi > M_{S_1}$ and $M_\Psi > M_{S_2} > M_{S_1}$. We consider two boosted tops associated with missing transverse momentum as our signal. It is interesting to note that the significance of the former hierarchy is always greater or equal to the second. In the case of the former, S_2 can decay into $\Psi(\to S_1 j)j$ or $S_1 jj$ (through off-shell Ψ), where j is the up-type SM quark. If at least one of these jets is the top quark, then the signal efficiency increases and hence the significance. So the hierarchy $M_\Psi > M_{S_2} > M_{S_1}$ gives a lower statistical significance, and we consider this scenario throughout our result for a conservative estimation. The total number of events coming from the signal topology for different masses of S_2 and background events after applying an optimal cut ($\mathrm{BDT}_{\mathrm{opt}}$) is given in table 7 (lower) for the hierarchy $M_\Psi > M_{S_2} > M_{S_1}$. The statistical significance variation with the S_2 mass is also shown here for a given mass of Ψ and couplings. The mass of S_2 has no effect on the statistical significance of the boosted top fatjets plus a large missing momentum signature. However, if one of the decay products of S_2 ($S_2 \to S_1 jj$) is at least a top quark, then it can increase the significance.

JHEP12(2022)167

BP	N_S^{bc}	BD$T_{\rm opt}$	N_S	N_B	σ	$\frac{N_S}{N_B}$ (MVA)	$\frac{N_S}{N_B}$ (CBA)
BP1	6625	-0.0259	5643	8584	47.3	0.66	0.41
BP2	3525	0.1584	2325	2047	35.1	1.14	0.47
BP3	2341	0.2553	1222	1048	25.6	1.17	0.40
BP4	2711	0.1975	1556	1277	29.2	1.22	0.35
BP5	2176	0.1446	1366	2502	21.9	0.55	0.23
BP6	1924	0.1325	1170	2727	18.7	0.43	0.17
BP7	1424	0.1398	821	2845	13.6	0.29	0.13
BP8	1081	0.0942	624	2951	10.4	0.21	0.12
BP9	915	0.0785	627	4820	8.5	0.13	0.08
BP10	552	0.0506	311	3469	5.0	0.09	0.04
BP11	385	0.3875	134	346	6.1	0.39	0.09
$N_{\rm SM}$	19246						

ΔM (GeV)	N_S^{bc}	BD$T_{\rm opt}$	N_S	N_B	$\sigma = \frac{N_S}{\sqrt{N_S+N_B}}$
75.1	2315	0.2645	1252	1240	25.1
100 (BP3)	2341	0.2553	1222	1048	25.6
153.6	2258	0.2129	1246	1176	25.3
200.4	2035	0.1899	1284	1384	24.9
244.5	2019	0.2963	1159	948	25.2
302.7	2036	0.208	1254	1240	25.1
351	2034	0.2271	1261	1199	25.4
402.7	2023	0.2778	1133	882	25.2
$N_{\rm SM}$	19246				

Table 7. The upper table demonstrates the effectiveness of the current search in terms of statistical significance (σ) for different benchmark points conceived for this study. The lower table illustrates the variation of this potential for one benchmark point, changing the mass of the heavy scalar, S_2, and shows that this mass does not have much impact in exploring the parameter space. N_S^{bc} and $N_{\rm SM}$ are the total number of events for different signal benchmark points and the combined background before applying any cut on BDT output (as shown in table 6). After using an optimal selection on the BDT response (BD$T_{\rm opt}$) surviving number of signal and background events are given by N_S and N_B, respectively for 14 TeV LHC for an integrated luminosity 139 fb^{-1}. Corresponding statistical significance and the signal-to-background ratio are also presented for ready reference. To better compare the sensitivities between the different analysis methods, we add the $\frac{N_S}{N_B}$ ratio of CBA from table 5 in the last column of the upper table.

JHEP12(2022)167

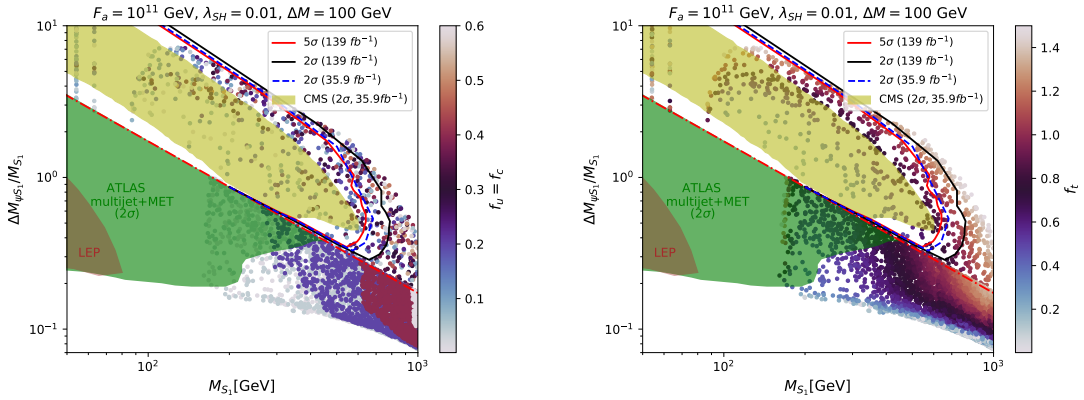

Figure 10. The solid red line is the 5σ discovery contour, and any point inside the red line has a statistical significance $> 5\sigma$ at 14 TeV LHC for an integrated luminosity 139 fb^{-1}. The dashed red line corresponds to $\Delta M_{\Psi S_1} = M_\Psi - M_{S_1} = M_{\rm top}$. Below the dashed red line, we can not probe with the boosted tops plus missing energy signal, as we can not get any on-shell top from the decay of Ψ. The solid black and blue dashed lines are the exclusion contour (2σ) of our analysis for an integrated luminosity of 139 fb^{-1} and 35.9 fb^{-1}, respectively. The exclusion region (2σ) from the existing LEP, ATLAS (multijet + MET), and CMS ($t\bar{t}$ + MET) analysis are shown by brown, green, and olive color, respectively.

Finally, we present the discovery (5σ) and exclusion (2σ) contours from our analysis at 14 TeV LHC for an integrated luminosity 139 fb^{-1} in the bi-dimensional plane of $\dfrac{\Delta M_{\Psi S_1}}{M_{S_1}} - M_{S_1}$ in figure 10 by solid red and solid black lines, respectively. Our analysis is effective when the on-shell top is produced from Ψ decay. Hence the region below the dashed red line can not be probed in the present channel. Considering the 100% branching fraction of the decay of Ψ into the top quark associated with the scalar, the existing search [86] can exclude vector-like quark masses up to 1 TeV. We find the masses of the vector-like quark ranging up to 1.41 TeV can be excluded, while the masses extent to 1.28 TeV can be discovered at 14 TeV LHC with an integrated luminosity of 139 fb^{-1}. In the region below the dashed red line, the mass difference between a vector-like quark and the scalar DM is less than the top quark's mass, and the vector-like quark fully decays into a light quark associated with a scalar when kinematically allowed. So, one can probe those regions using multi jets plus missing transverse momentum signature, which is beyond the scope of our present analysis.

6 Summary and conclusion

In this work, we analyze a hybrid KSVZ setup, where the model is extended by an extra complex scalar singlet whose lightest component plays the role of dark matter. We highlight the fact that the presence of a colored vector-like quark that occurs naturally in the KSVZ model plays a crucial role both in the dark sector and collider phenomenology of the setup. Being charged under U(1)$_{\rm PQ}$ allows the VLQ to couple with all up-type quarks and the DM through the Yukawa interactions. When appropriately tuned, this coupling can enhance the

JHEP12(2022)167

DM parameter space in comparison to what is observed in a pure scalar singlet DM scenario. In this work, we demonstrate that the Yukawa couplings play a non-trivial role in obtaining the observed relic density. Moreover, the same couplings also allow the parameter space from the direct search bounds by entering into extra Feynman diagrams that contribute toward the direct detection cross-section of the dark matter.

A search of vector-like quarks in events with two boosted top fatjets with large missing transverse momentum is presented. The analysis is done for 139 fb^{-1} integrated luminosity at 14 TeV LHC. We discuss all the significant backgrounds that can potentially mimic the signal. Jet substructure variables and various other variables are used in our analysis. Sophisticated multivariate analysis is performed to increase the sensitivity over cut-based one. Different jet substructure variables, $\Delta R(J_0, J_1)$, N-subjettiness ratios, and M_{eff} are outstanding in distinguishing the signal from the background and take a central role in getting very high significance. However, the missing transverse momentum distribution and the azimuthal separation between the subleading fatjet and the missing transverse energy direction have the uppermost importance in separating the signal from the background. With a conservative estimation, we give discovery and exclusion contours in figure 10 in the region where the mass difference between the vector-like quark and the scalar dark matter is larger than the top quark mass.

Acknowledgments

This work is supported by the Physical Research Laboratory (PRL), Department of Space, Government of India. Computational work was performed using the HPC resources (Vikram-100 HPC) and TDP project at PRL. R.R. also acknowledges the National Research Foundation of Korea (NRF) grant funded by the Korean government (NRF-2020R1C1C1012452).

JHEP12(2022)167

A Feynman diagrams

- Annihilation channels of scalar dark matter S_1 are shown in figure 11.
- Co-annihilation channels of scalar dark matter S_1 are shown in figure 12.
- Annihilation channels of vector-like quark Ψ are shown in figure 13.
- Spin independent elastic scattering between dark matter (S_1) and nucleon channels are shown in figure 14.
- Diagrams contributing to the $D^0 - \bar{D}^0$ mixing are shown in figure 15.

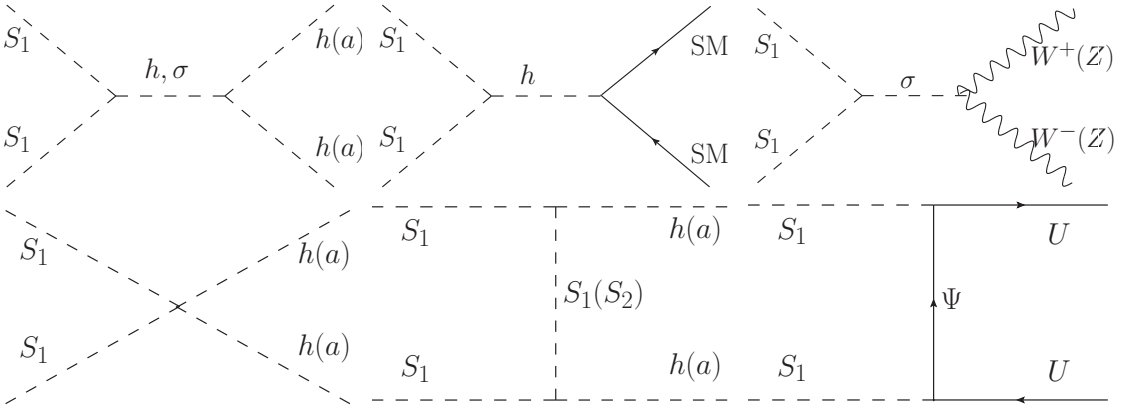

Figure 11. Annihilation channels of scalar dark matter S_1. U denotes the SM up-type quark ($U \equiv u, c, t, \bar{u}, \bar{c}, \bar{t}$).

JHEP12(2022)167

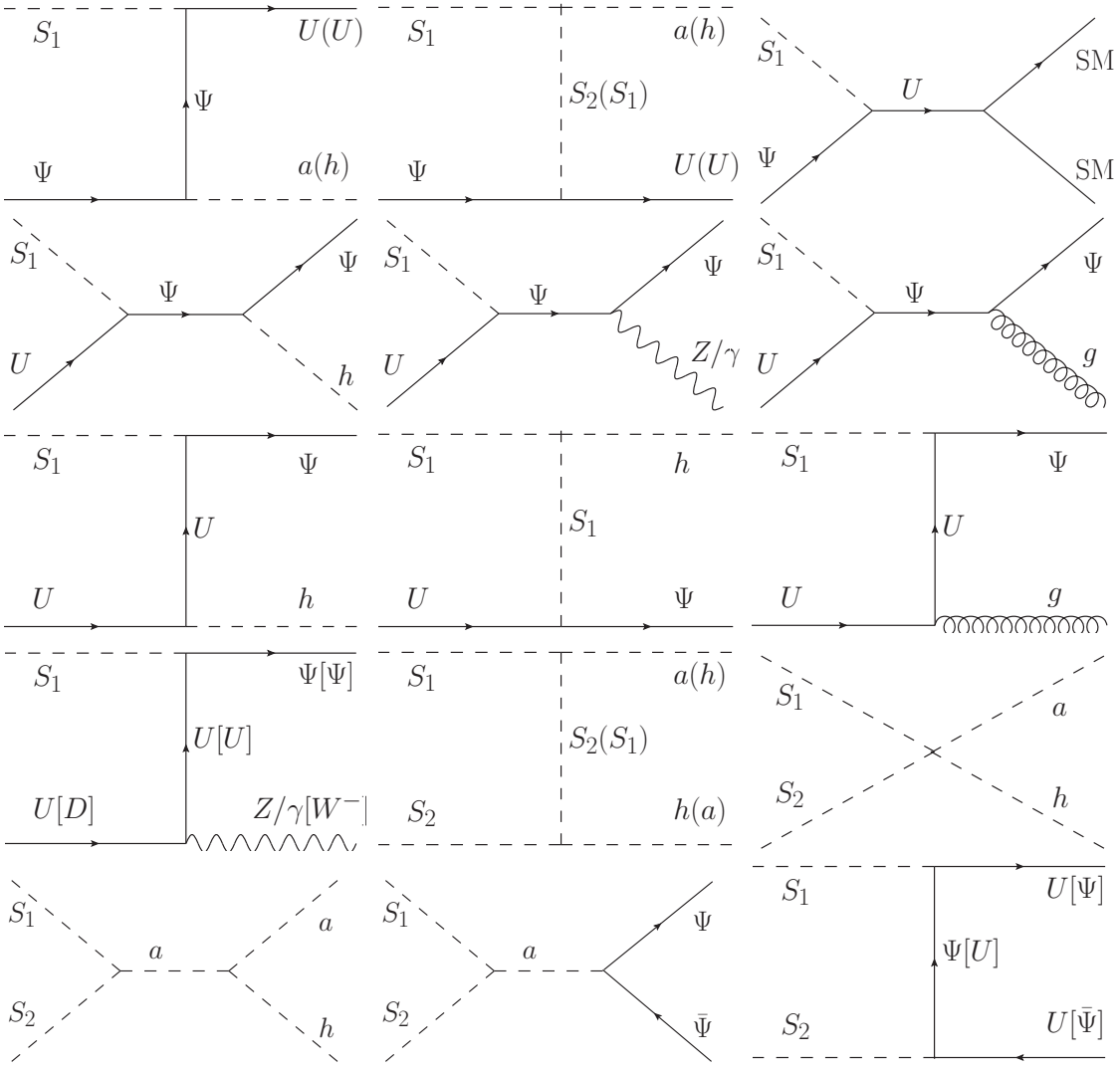

Figure 12. Co-annihilation channels of scalar dark matter S_1. U and D denote the SM up-type and down-type quark, respectively; $U \equiv u, c, t, \bar{u}, \bar{c}, \bar{t},\ D \equiv d, s, b, \bar{d}, \bar{s}, \bar{b}$.

JHEP12(2022)167

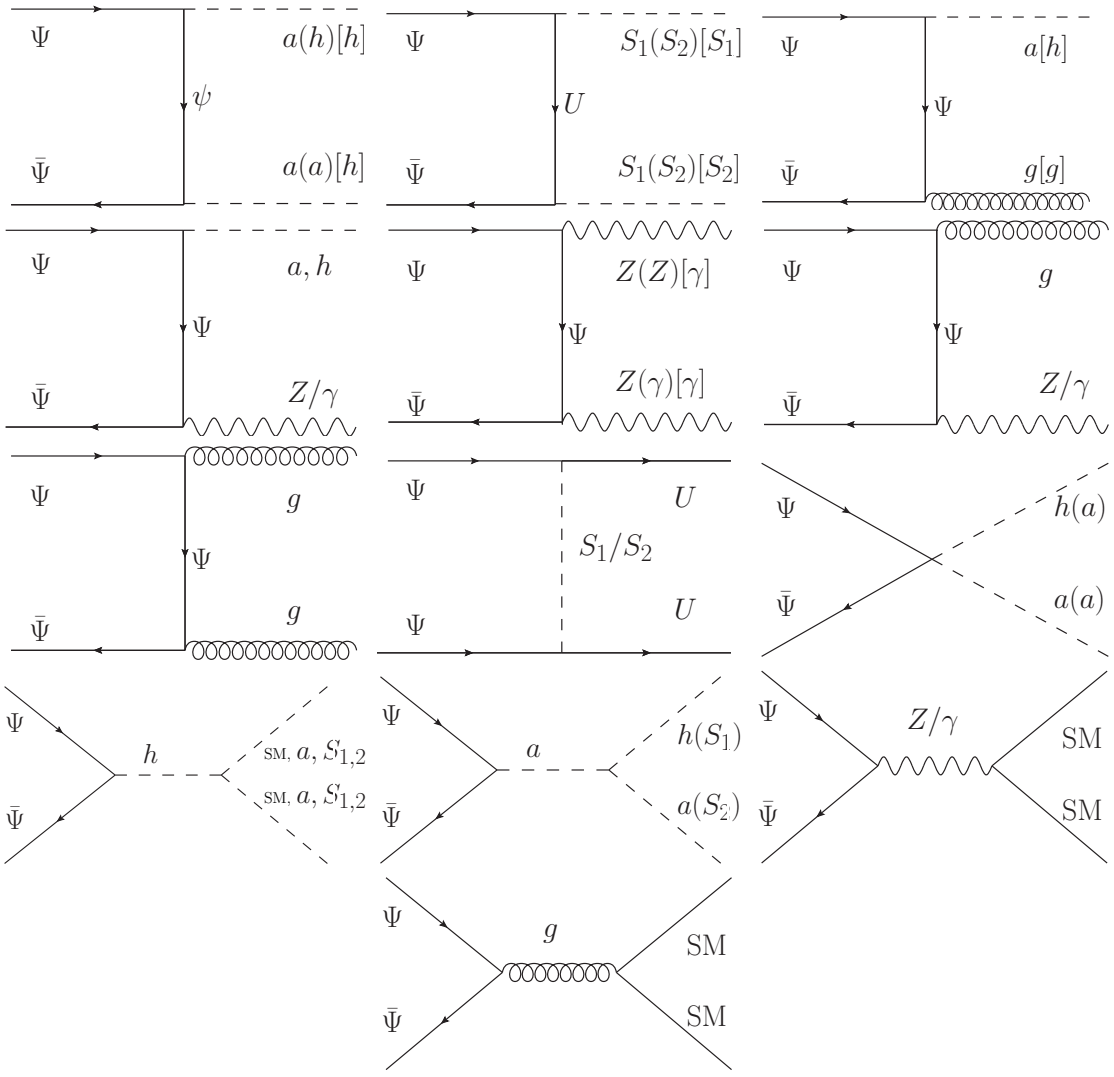

Figure 13. Annihilation channels of vectorlike quark Ψ. U denotes the SM up-type quark ($U \equiv u, c, t, \bar{u}, \bar{c}, \bar{t}$).

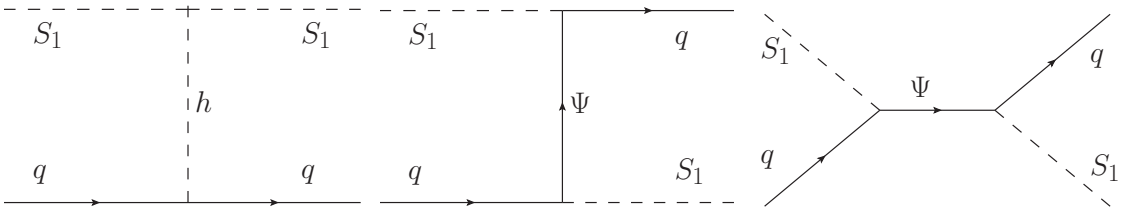

Figure 14. Spin independent elastic scattering between dark matter (S_1) and nucleon.

JHEP12(2022)167

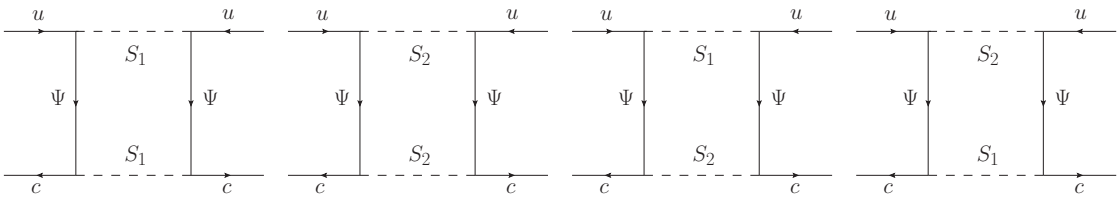

Figure 15. Diagrams contributing to the $D^0 - \bar{D}^0$ mixing.

JHEP12(2022)167

References

[1] CMS collaboration, *Observation of a New Boson at a Mass of 125 GeV with the CMS Experiment at the LHC*, *Phys. Lett. B* **716** (2012) 30 [arXiv:1207.7235] [INSPIRE].

[2] ATLAS collaboration, *Observation of a new particle in the search for the Standard Model Higgs boson with the ATLAS detector at the LHC*, *Phys. Lett. B* **716** (2012) 1 [arXiv:1207.7214] [INSPIRE].

[3] R.D. Peccei and H.R. Quinn, *CP Conservation in the Presence of Instantons*, *Phys. Rev. Lett.* **38** (1977) 1440 [INSPIRE].

[4] R.D. Peccei and H.R. Quinn, *Constraints Imposed by CP Conservation in the Presence of Instantons*, *Phys. Rev. D* **16** (1977) 1791 [INSPIRE].

[5] Y. Sofue and V. Rubin, *Rotation curves of spiral galaxies*, *Ann. Rev. Astron. Astrophys.* **39** (2001) 137 [astro-ph/0010594] [INSPIRE].

[6] D. Clowe et al., *A direct empirical proof of the existence of dark matter*, *Astrophys. J. Lett.* **648** (2006) L109 [astro-ph/0608407] [INSPIRE].

[7] SUPER-KAMIOKANDE collaboration, *Evidence for oscillation of atmospheric neutrinos*, *Phys. Rev. Lett.* **81** (1998) 1562 [hep-ex/9807003] [INSPIRE].

[8] SNO collaboration, *Direct evidence for neutrino flavor transformation from neutral current interactions in the Sudbury Neutrino Observatory*, *Phys. Rev. Lett.* **89** (2002) 011301 [nucl-ex/0204008] [INSPIRE].

[9] K2K collaboration, *Indications of neutrino oscillation in a 250 km long baseline experiment*, *Phys. Rev. Lett.* **90** (2003) 041801 [hep-ex/0212007] [INSPIRE].

[10] A. Riotto and M. Trodden, *Recent progress in baryogenesis*, *Ann. Rev. Nucl. Part. Sci.* **49** (1999) 35 [hep-ph/9901362] [INSPIRE].

[11] M. Dine and A. Kusenko, *The origin of the matter-antimatter asymmetry*, *Rev. Mod. Phys.* **76** (2003) 1 [hep-ph/0303065] [INSPIRE].

[12] WMAP collaboration, *Nine-Year Wilkinson Microwave Anisotropy Probe (WMAP) Observations: Cosmological Parameter Results*, *Astrophys. J. Suppl.* **208** (2013) 19 [arXiv:1212.5226] [INSPIRE].

[13] Planck collaboration, *Planck 2018 results. X. Constraints on inflation*, *Astron. Astrophys.* **641** (2020) A10 [arXiv:1807.06211] [INSPIRE].

[14] G. Jungman, M. Kamionkowski and K. Griest, *Supersymmetric dark matter*, *Phys. Rept.* **267** (1996) 195 [hep-ph/9506380] [INSPIRE].

[15] G. Bertone, D. Hooper and J. Silk, *Particle dark matter: Evidence, candidates and constraints*, *Phys. Rept.* **405** (2005) 279 [hep-ph/0404175] [INSPIRE].

[16] P. Konar, K. Kong, K.T. Matchev and M. Perelstein, *Shedding Light on the Dark Sector with Direct WIMP Production*, *New J. Phys.* **11** (2009) 105004 [arXiv:0902.2000] [INSPIRE].

[17] J.L. Feng, *Dark Matter Candidates from Particle Physics and Methods of Detection*, *Ann. Rev. Astron. Astrophys.* **48** (2010) 495 [arXiv:1003.0904] [INSPIRE].

[18] G. Arcadi et al., *The waning of the WIMP? A review of models, searches, and constraints*, *Eur. Phys. J. C* **78** (2018) 203 [arXiv:1703.07364] [INSPIRE].

[19] A. Ghosh, P. Konar and S. Seth, *Precise probing of the inert Higgs-doublet model at the LHC*, *Phys. Rev. D* **105** (2022) 115038 [arXiv:2111.15236] [INSPIRE].

[20] P. Konar, A. Mukherjee, A.K. Saha and S. Show, *Linking pseudo-Dirac dark matter to radiative neutrino masses in a singlet-doublet scenario*, *Phys. Rev. D* **102** (2020) 015024 [arXiv:2001.11325] [INSPIRE].

[21] P. Konar, A. Mukherjee, A.K. Saha and S. Show, *A dark clue to seesaw and leptogenesis in a pseudo-Dirac singlet doublet scenario with (non)standard cosmology*, *JHEP* **03** (2021) 044 [arXiv:2007.15608] [INSPIRE].

[22] L.J. Hall, K. Jedamzik, J. March-Russell and S.M. West, *Freeze-In Production of FIMP Dark Matter*, *JHEP* **03** (2010) 080 [arXiv:0911.1120] [INSPIRE].

[23] N. Bernal, M. Heikinheimo, T. Tenkanen, K. Tuominen and V. Vaskonen, *The Dawn of FIMP Dark Matter: A Review of Models and Constraints*, *Int. J. Mod. Phys. A* **32** (2017) 1730023 [arXiv:1706.07442] [INSPIRE].

[24] B. Barman, D. Borah and R. Roshan, *Effective Theory of Freeze-in Dark Matter*, *JCAP* **11** (2020) 021 [arXiv:2007.08768] [INSPIRE].

[25] B. Barman, D. Borah and R. Roshan, *Nonthermal leptogenesis and UV freeze-in of dark matter: Impact of inflationary reheating*, *Phys. Rev. D* **104** (2021) 035022 [arXiv:2103.01675] [INSPIRE].

[26] A. Datta, R. Roshan and A. Sil, *Imprint of the Seesaw Mechanism on Feebly Interacting Dark Matter and the Baryon Asymmetry*, *Phys. Rev. Lett.* **127** (2021) 231801 [arXiv:2104.02030] [INSPIRE].

[27] B. Barman, N. Bernal, A. Das and R. Roshan, *Non-minimally coupled vector boson dark matter*, *JCAP* **01** (2022) 047 [arXiv:2108.13447] [INSPIRE].

[28] P. Konar, R. Roshan and S. Show, *Freeze-in dark matter through forbidden channel in* U(1)$B - L$, *JCAP* **03** (2022) 021 [arXiv:2110.14411] [INSPIRE].

[29] N. Chakrabarty, P. Konar, R. Roshan and S. Show, *Thermally corrected masses and freeze-in dark matter: a case study*, arXiv:2206.02233 [INSPIRE].

[30] A. Dutta Banik, R. Roshan and A. Sil, *Neutrino mass and asymmetric dark matter: study with inert Higgs doublet and high scale validity*, *JCAP* **03** (2021) 037 [arXiv:2011.04371] [INSPIRE].

JHEP12(2022)167

[31] B. Barman, D. Borah, S.J. Das and R. Roshan, *Non-thermal origin of asymmetric dark matter from inflaton and primordial black holes*, *JCAP* **03** (2022) 031 [arXiv:2111.08034] [INSPIRE].

[32] J. Preskill, M.B. Wise and F. Wilczek, *Cosmology of the Invisible Axion*, *Phys. Lett. B* **120** (1983) 127 [INSPIRE].

[33] L.F. Abbott and P. Sikivie, *A Cosmological Bound on the Invisible Axion*, *Phys. Lett. B* **120** (1983) 133 [INSPIRE].

[34] M. Dine and W. Fischler, *The Not So Harmless Axion*, *Phys. Lett. B* **120** (1983) 137 [INSPIRE].

[35] D.J.E. Marsh, *Axion Cosmology*, *Phys. Rept.* **643** (2016) 1 [arXiv:1510.07633] [INSPIRE].

[36] F. Kahlhoefer, *Review of LHC Dark Matter Searches*, *Int. J. Mod. Phys. A* **32** (2017) 1730006 [arXiv:1702.02430] [INSPIRE].

[37] CMS collaboration, *Search for dark matter produced in association with heavy-flavor quark pairs in proton-proton collisions at* $\sqrt{s} = 13$ *TeV*, *Eur. Phys. J. C* **77** (2017) 845 [arXiv:1706.02581] [INSPIRE].

[38] LUX collaboration, *Results from a search for dark matter in the complete LUX exposure*, *Phys. Rev. Lett.* **118** (2017) 021303 [arXiv:1608.07648] [INSPIRE].

[39] PandaX-II collaboration, *Dark Matter Results from First 98.7 Days of Data from the PandaX-II Experiment*, *Phys. Rev. Lett.* **117** (2016) 121303 [arXiv:1607.07400] [INSPIRE].

[40] PandaX-II collaboration, *Dark Matter Results From 54-Ton-Day Exposure of PandaX-II Experiment*, *Phys. Rev. Lett.* **119** (2017) 181302 [arXiv:1708.06917] [INSPIRE].

[41] XENON collaboration, *Dark Matter Search Results from a One Ton-Year Exposure of XENON1T*, *Phys. Rev. Lett.* **121** (2018) 111302 [arXiv:1805.12562] [INSPIRE].

[42] K. Kohri, A. Mazumdar, N. Sahu and P. Stephens, *Probing Unified Origin of Dark Matter and Baryon Asymmetry at PAMELA/Fermi*, *Phys. Rev. D* **80** (2009) 061302 [arXiv:0907.0622] [INSPIRE].

[43] MAGIC and Fermi-LAT collaborations, *Limits to Dark Matter Annihilation Cross-Section from a Combined Analysis of MAGIC and Fermi-LAT Observations of Dwarf Satellite Galaxies*, *JCAP* **02** (2016) 039 [arXiv:1601.06590] [INSPIRE].

[44] B. Eiteneuer, A. Goudelis and J. Heisig, *The inert doublet model in the light of Fermi-LAT gamma-ray data: a global fit analysis*, *Eur. Phys. J. C* **77** (2017) 624 [arXiv:1705.01458] [INSPIRE].

[45] D. Borah, R. Roshan and A. Sil, *Minimal two-component scalar doublet dark matter with radiative neutrino mass*, *Phys. Rev. D* **100** (2019) 055027 [arXiv:1904.04837] [INSPIRE].

[46] S. Bhattacharya, P. Ghosh, A.K. Saha and A. Sil, *Two component dark matter with inert Higgs doublet: neutrino mass, high scale validity and collider searches*, *JHEP* **03** (2020) 090 [arXiv:1905.12583] [INSPIRE].

[47] S. Bhattacharya, N. Chakrabarty, R. Roshan and A. Sil, *Multicomponent dark matter in extended* $\mathrm{U}(1)_{B-L}$*: neutrino mass and high scale validity*, *JCAP* **04** (2020) 013 [arXiv:1910.00612] [INSPIRE].

[48] A. Dutta Banik, R. Roshan and A. Sil, *Two component singlet-triplet scalar dark matter and electroweak vacuum stability*, *Phys. Rev. D* **103** (2021) 075001 [arXiv:2009.01262] [INSPIRE].

JHEP12(2022)167

[49] N. Chakrabarty, R. Roshan and A. Sil, *Two-component doublet-triplet scalar dark matter stabilizing the electroweak vacuum*, *Phys. Rev. D* **105** (2022) 115010 [arXiv:2102.06032] [INSPIRE].

[50] A. Dutta Banik, M. Pandey, D. Majumdar and A. Biswas, *Two component WIMP-FImP dark matter model with singlet fermion, scalar and pseudo scalar*, *Eur. Phys. J. C* **77** (2017) 657 [arXiv:1612.08621] [INSPIRE].

[51] D. Borah, A. Dasgupta and S.K. Kang, *Two-component dark matter with cogenesis of the baryon asymmetry of the Universe*, *Phys. Rev. D* **100** (2019) 103502 [arXiv:1903.10516] [INSPIRE].

[52] S. Bhattacharya, S. Chakraborti and D. Pradhan, *Electroweak symmetry breaking and WIMP-FIMP dark matter*, *JHEP* **07** (2022) 091 [arXiv:2110.06985] [INSPIRE].

[53] W. Abdallah, S. Choubey and S. Khan, *FIMP dark matter candidate(s) in a $B-L$ model with inverse seesaw mechanism*, *JHEP* **06** (2019) 095 [arXiv:1904.10015] [INSPIRE].

[54] M. Pandey and A. Paul, *Gravitational Wave Emissions from First Order Phase Transitions with Two Component FIMP Dark Matter*, arXiv:2003.08828 [INSPIRE].

[55] B. Dasgupta, E. Ma and K. Tsumura, *Weakly interacting massive particle dark matter and radiative neutrino mass from Peccei-Quinn symmetry*, *Phys. Rev. D* **89** (2014) 041702 [arXiv:1308.4138] [INSPIRE].

[56] S. Chatterjee, A. Das, T. Samui and M. Sen, *Mixed WIMP-axion dark matter*, *Phys. Rev. D* **100** (2019) 115050 [arXiv:1810.09471] [INSPIRE].

[57] G. Lazarides, R. Maji, R. Roshan and Q. Shafi, *Heavier W boson, dark matter, and gravitational waves from strings in an* SO(10) *axion model*, *Phys. Rev. D* **106** (2022) 055009 [arXiv:2205.04824] [INSPIRE].

[58] P. Konar, K. Kong, K.T. Matchev and M. Park, *Dark Matter Particle Spectroscopy at the LHC: Generalizing M(T2) to Asymmetric Event Topologies*, *JHEP* **04** (2010) 086 [arXiv:0911.4126] [INSPIRE].

[59] V. Silveira and A. Zee, *Scalar phantoms*, *Phys. Lett. B* **161** (1985) 136 [INSPIRE].

[60] J. McDonald, *Gauge singlet scalars as cold dark matter*, *Phys. Rev. D* **50** (1994) 3637 [hep-ph/0702143] [INSPIRE].

[61] C.P. Burgess, M. Pospelov and T. ter Veldhuis, *The minimal model of nonbaryonic dark matter: A singlet scalar*, *Nucl. Phys. B* **619** (2001) 709 [hep-ph/0011335] [INSPIRE].

[62] D. Borah, R. Roshan and A. Sil, *Sub-TeV singlet scalar dark matter and electroweak vacuum stability with vectorlike fermions*, *Phys. Rev. D* **102** (2020) 075034 [arXiv:2007.14904] [INSPIRE].

[63] F. Wilczek, *Problem of Strong P and T Invariance in the Presence of Instantons*, *Phys. Rev. Lett.* **40** (1978) 279 [INSPIRE].

[64] S. Weinberg, *A New Light Boson?*, *Phys. Rev. Lett.* **40** (1978) 223 [INSPIRE].

[65] J.E. Kim, *Weak Interaction Singlet and Strong CP Invariance*, *Phys. Rev. Lett.* **43** (1979) 103 [INSPIRE].

[66] M.A. Shifman, A.I. Vainshtein and V.I. Zakharov, *Can Confinement Ensure Natural CP Invariance of Strong Interactions?*, *Nucl. Phys. B* **166** (1980) 493 [INSPIRE].

JHEP12(2022)167

[67] M. Dine, W. Fischler and M. Srednicki, *A Simple Solution to the Strong CP Problem with a Harmless Axion*, *Phys. Lett. B* **104** (1981) 199 [INSPIRE].

[68] A.R. Zhitnitsky, *On Possible Suppression of the Axion Hadron Interactions* (In Russian), *Sov. J. Nucl. Phys.* **31** (1980) 260 [INSPIRE].

[69] PLANCK collaboration, *Planck 2018 results. VI. Cosmological parameters*, *Astron. Astrophys.* **641** (2020) A6 [arXiv:1807.06209] [INSPIRE].

[70] M. Garny, A. Ibarra, S. Rydbeck and S. Vogl, *Majorana Dark Matter with a Coloured Mediator: Collider vs Direct and Indirect Searches*, *JHEP* **06** (2014) 169 [arXiv:1403.4634] [INSPIRE].

[71] O. Gedalia, Y. Grossman, Y. Nir and G. Perez, *Lessons from Recent Measurements of D0-anti-D0 Mixing*, *Phys. Rev. D* **80** (2009) 055024 [arXiv:0906.1879] [INSPIRE].

[72] T. Robens and T. Stefaniak, *LHC Benchmark Scenarios for the Real Higgs Singlet Extension of the Standard Model*, *Eur. Phys. J. C* **76** (2016) 268 [arXiv:1601.07880] [INSPIRE].

[73] ATLAS collaboration, *Combination of searches for invisible Higgs boson decays with the ATLAS experiment*, [INSPIRE].

[74] F. Giacchino, A. Ibarra, L. Lopez Honorez, M.H.G. Tytgat and S. Wild, *Signatures from Scalar Dark Matter with a Vector-like Quark Mediator*, *JCAP* **02** (2016) 002 [arXiv:1511.04452] [INSPIRE].

[75] OPAL collaboration, *Search for scalar top and scalar bottom quarks at LEP*, *Phys. Lett. B* **545** (2002) 272 [hep-ex/0209026] [INSPIRE].

[76] ATLAS collaboration, *Search for squarks and gluinos with the ATLAS detector in final states with jets and missing transverse momentum using 20.3 fb^{-1} of $\sqrt{s} = 8$ TeV proton-proton collision data*, in *2nd Large Hadron Collider Physics Conference*2014 [arXiv:1408.5857] [INSPIRE].

[77] ATLAS collaboration, *Search for top-squark pair production in final states with one lepton, jets, and missing transverse momentum using 36 fb^{-1} of $\sqrt{s} = 13$ TeV pp collision data with the ATLAS detector*, *JHEP* **06** (2018) 108 [arXiv:1711.11520] [INSPIRE].

[78] ATLAS collaboration, *Search for a scalar partner of the top quark in the jets plus missing transverse momentum final state at $\sqrt{s} = 13$ TeV with the ATLAS detector*, *JHEP* **12** (2017) 085 [arXiv:1709.04183] [INSPIRE].

[79] ATLAS collaboration, *Search for supersymmetry in events with b-tagged jets and missing transverse momentum in pp collisions at $\sqrt{s} = 13$ TeV with the ATLAS detector*, *JHEP* **11** (2017) 195 [arXiv:1708.09266] [INSPIRE].

[80] ATLAS collaboration, *Search for direct top squark pair production in final states with two leptons in $\sqrt{s} = 13$ TeV pp collisions with the ATLAS detector*, *Eur. Phys. J. C* **77** (2017) 898 [arXiv:1708.03247] [INSPIRE].

[81] ATLAS collaboration, *Search for supersymmetry in final states with two same-sign or three leptons and jets using 36 fb^{-1} of $\sqrt{s} = 13$ TeV pp collision data with the ATLAS detector*, *JHEP* **09** (2017) 084 [arXiv:1706.03731] [INSPIRE].

[82] CMS collaboration, *Search for new phenomena with the M_{T2} variable in the all-hadronic final state produced in proton-proton collisions at $\sqrt{s} = 13$ TeV*, *Eur. Phys. J. C* **77** (2017) 710 [arXiv:1705.04650] [INSPIRE].

JHEP12(2022)167

[83] CMS collaboration, *Search for direct production of supersymmetric partners of the top quark in the all-jets final state in proton-proton collisions at* $\sqrt{s} = 13$ *TeV*, *JHEP* **10** (2017) 005 [arXiv:1707.03316] [INSPIRE].

[84] CMS collaboration, *Search for top squark pair production in pp collisions at* $\sqrt{s} = 13$ *TeV using single lepton events*, *JHEP* **10** (2017) 019 [arXiv:1706.04402] [INSPIRE].

[85] CMS collaboration, *Search for top squarks and dark matter particles in opposite-charge dilepton final states at* $\sqrt{s} = 13$ *TeV*, *Phys. Rev. D* **97** (2018) 032009 [arXiv:1711.00752] [INSPIRE].

[86] S. Colucci, B. Fuks, F. Giacchino, L. Lopez Honorez, M.H.G. Tytgat and J. Vandecasteele, *Top-philic Vector-Like Portal to Scalar Dark Matter*, *Phys. Rev. D* **98** (2018) 035002 [arXiv:1804.05068] [INSPIRE].

[87] K.J. Bae, J.-H. Huh and J.E. Kim, *Update of axion CDM energy*, *JCAP* **09** (2008) 005 [arXiv:0806.0497] [INSPIRE].

[88] A. Alloul, N.D. Christensen, C. Degrande, C. Duhr and B. Fuks, *FeynRules 2.0 — A complete toolbox for tree-level phenomenology*, *Comput. Phys. Commun.* **185** (2014) 2250 [arXiv:1310.1921] [INSPIRE].

[89] G. Bélanger, F. Boudjema, A. Goudelis, A. Pukhov and B. Zaldivar, *micrOMEGAs5.0: Freeze-in*, *Comput. Phys. Commun.* **231** (2018) 173 [arXiv:1801.03509] [INSPIRE].

[90] ADMX collaboration, *A SQUID-based microwave cavity search for dark-matter axions*, *Phys. Rev. Lett.* **104** (2010) 041301 [arXiv:0910.5914] [INSPIRE].

[91] D. Budker, P.W. Graham, M. Ledbetter, S. Rajendran and A. Sushkov, *Proposal for a Cosmic Axion Spin Precession Experiment (CASPEr)*, *Phys. Rev. X* **4** (2014) 021030 [arXiv:1306.6089] [INSPIRE].

[92] Y. Kahn, B.R. Safdi and J. Thaler, *Broadband and Resonant Approaches to Axion Dark Matter Detection*, *Phys. Rev. Lett.* **117** (2016) 141801 [arXiv:1602.01086] [INSPIRE].

[93] MADMAX Working Group collaboration, *Dielectric Haloscopes: A New Way to Detect Axion Dark Matter*, *Phys. Rev. Lett.* **118** (2017) 091801 [arXiv:1611.05865] [INSPIRE].

[94] G. Raffelt and D. Seckel, *Bounds on Exotic Particle Interactions from SN 1987a*, *Phys. Rev. Lett.* **60** (1988) 1793 [INSPIRE].

[95] S. Profumo, L. Giani and O.F. Piattella, *An Introduction to Particle Dark Matter*, *Universe* **5** (2019) 213 [arXiv:1910.05610] [INSPIRE].

[96] F.F. Deppisch, W. Liu and M. Mitra, *Long-lived Heavy Neutrinos from Higgs Decays*, *JHEP* **08** (2018) 181 [arXiv:1804.04075] [INSPIRE].

[97] S. Baek, P. Ko and P. Wu, *Top-philic Scalar Dark Matter with a Vector-like Fermionic Top Partner*, *JHEP* **10** (2016) 117 [arXiv:1606.00072] [INSPIRE].

[98] A. Das, P. Konar and A. Thalapillil, *Jet substructure shedding light on heavy Majorana neutrinos at the LHC*, *JHEP* **02** (2018) 083 [arXiv:1709.09712] [INSPIRE].

[99] A. Bhardwaj, A. Das, P. Konar and A. Thalapillil, *Looking for Minimal Inverse Seesaw scenarios at the LHC with Jet Substructure Techniques*, *J. Phys. G* **47** (2020) 075002 [arXiv:1801.00797] [INSPIRE].

[100] A. Bhardwaj, P. Konar, T. Mandal and S. Sadhukhan, *Probing the inert doublet model using jet substructure with a multivariate analysis*, *Phys. Rev. D* **100** (2019) 055040 [arXiv:1905.04195] [INSPIRE].

JHEP12(2022)167

[101] A. Bhardwaj, J. Dutta, P. Konar, B. Mukhopadhyaya and S.K. Rai, *Boosted jet techniques for a supersymmetric scenario with gravitino LSP*, *JHEP* **10** (2020) 083 [arXiv:2007.00351] [INSPIRE].

[102] J. Alwall et al., *The automated computation of tree-level and next-to-leading order differential cross sections, and their matching to parton shower simulations*, *JHEP* **07** (2014) 079 [arXiv:1405.0301] [INSPIRE].

[103] T. Sjöstrand, L. Lonnblad and S. Mrenna, *PYTHIA 6.2: Physics and manual*, hep-ph/0108264 [INSPIRE].

[104] T. Sjöstrand et al., *An introduction to PYTHIA 8.2*, *Comput. Phys. Commun.* **191** (2015) 159 [arXiv:1410.3012] [INSPIRE].

[105] M.L. Mangano, M. Moretti, F. Piccinini and M. Treccani, *Matching matrix elements and shower evolution for top-quark production in hadronic collisions*, *JHEP* **01** (2007) 013 [hep-ph/0611129] [INSPIRE].

[106] S. Hoeche et al., *Matching parton showers and matrix elements*, in *HERA and the LHC: A Workshop on the Implications of HERA for LHC Physics: CERN — DESY Workshop 2004/2005 (Midterm Meeting, CERN, 11–13 October 2004; Final Meeting, DESY, 17–21 January 2005)*, pp. 288–2892005, DOI [hep-ph/0602031] [INSPIRE].

[107] DELPHES 3 collaboration, *DELPHES 3, A modular framework for fast simulation of a generic collider experiment*, *JHEP* **02** (2014) 057 [arXiv:1307.6346] [INSPIRE].

[108] M. Cacciari, G.P. Salam and G. Soyez, *The anti-k_t jet clustering algorithm*, *JHEP* **04** (2008) 063 [arXiv:0802.1189] [INSPIRE].

[109] Y.L. Dokshitzer, G.D. Leder, S. Moretti and B.R. Webber, *Better jet clustering algorithms*, *JHEP* **08** (1997) 001 [hep-ph/9707323] [INSPIRE].

[110] M. Cacciari, G.P. Salam and G. Soyez, *FastJet User Manual*, *Eur. Phys. J. C* **72** (2012) 1896 [arXiv:1111.6097] [INSPIRE].

[111] A. Hocker et al., *TMVA — Toolkit for Multivariate Data Analysis*, physics/0703039 [INSPIRE].

[112] T. Plehn, M. Spannowsky, M. Takeuchi and D. Zerwas, *Stop Reconstruction with Tagged Tops*, *JHEP* **10** (2010) 078 [arXiv:1006.2833] [INSPIRE].

[113] C. Muselli, M. Bonvini, S. Forte, S. Marzani and G. Ridolfi, *Top Quark Pair Production beyond NNLO*, *JHEP* **08** (2015) 076 [arXiv:1505.02006] [INSPIRE].

[114] N. Kidonakis, *Theoretical results for electroweak-boson and single-top production*, *PoS* **DIS2015** (2015) 170 [arXiv:1506.04072] [INSPIRE].

[115] S. Catani, L. Cieri, G. Ferrera, D. de Florian and M. Grazzini, *Vector boson production at hadron colliders: a fully exclusive QCD calculation at NNLO*, *Phys. Rev. Lett.* **103** (2009) 082001 [arXiv:0903.2120] [INSPIRE].

[116] G. Balossini et al., *Combination of electroweak and QCD corrections to single W production at the Fermilab Tevatron and the CERN LHC*, *JHEP* **01** (2010) 013 [arXiv:0907.0276] [INSPIRE].

[117] J.M. Campbell, R.K. Ellis and C. Williams, *Vector boson pair production at the LHC*, *JHEP* **07** (2011) 018 [arXiv:1105.0020] [INSPIRE].

[118] J. Thaler and K. Van Tilburg, *Identifying Boosted Objects with N-subjettiness*, *JHEP* **03** (2011) 015 [arXiv:1011.2268] [INSPIRE].

JHEP12(2022)167

[119] J. Thaler and K. Van Tilburg, *Maximizing Boosted Top Identification by Minimizing N-subjettiness*, *JHEP* **02** (2012) 093 [arXiv:1108.2701] [INSPIRE].

[120] D. Krohn, J. Thaler and L.-T. Wang, *Jet Trimming*, *JHEP* **02** (2010) 084 [arXiv:0912.1342] [INSPIRE].

[121] J.M. Butterworth, A.R. Davison, M. Rubin and G.P. Salam, *Jet substructure as a new Higgs search channel at the LHC*, *Phys. Rev. Lett.* **100** (2008) 242001 [arXiv:0802.2470] [INSPIRE].

[122] S.D. Ellis, C.K. Vermilion and J.R. Walsh, *Techniques for improved heavy particle searches with jet substructure*, *Phys. Rev. D* **80** (2009) 051501 [arXiv:0903.5081] [INSPIRE].

[123] S.D. Ellis, C.K. Vermilion and J.R. Walsh, *Recombination Algorithms and Jet Substructure: Pruning as a Tool for Heavy Particle Searches*, *Phys. Rev. D* **81** (2010) 094023 [arXiv:0912.0033] [INSPIRE].

[124] C.G. Lester and D.J. Summers, *Measuring masses of semiinvisibly decaying particles pair produced at hadron colliders*, *Phys. Lett. B* **463** (1999) 99 [hep-ph/9906349] [INSPIRE].

[125] A.J. Barr et al., *Guide to transverse projections and mass-constraining variables*, *Phys. Rev. D* **84** (2011) 095031 [arXiv:1105.2977] [INSPIRE].

[126] P. Konar, K. Kong, K.T. Matchev and M. Park, *Superpartner Mass Measurement Technique using 1D Orthogonal Decompositions of the Cambridge Transverse Mass Variable M_{T2}*, *Phys. Rev. Lett.* **105** (2010) 051802 [arXiv:0910.3679] [INSPIRE].

[127] P. Konar, K. Kong and K.T. Matchev, *$\sqrt{\hat{s}}_{min}$: A global inclusive variable for determining the mass scale of new physics in events with missing energy at hadron colliders*, *JHEP* **03** (2009) 085 [arXiv:0812.1042] [INSPIRE].

[128] P. Konar, K. Kong, K.T. Matchev and M. Park, *RECO level $\sqrt{s}_{min}$ and subsystem $\sqrt{s}_{min}$: Improved global inclusive variables for measuring the new physics mass scale in E_T events at hadron colliders*, *JHEP* **06** (2011) 041 [arXiv:1006.0653] [INSPIRE].

JHEP12(2022)167